NUREG/CR-3980 Vol. III
ANL-84-61 Vol. Iii

NUREG/CR-3980 Vol. III
ANL-84-61 Vol. III

LIGHT-WATER-REACTOR SAFETY FUEL SYSTEMS RESEARCH PROGRAMS: QUARTERLY PROGRESS REPORT

July – September 1984

ARGONNE NATIONAL LABORATORY, ARGONNE, ILLINOIS
Operated by THE UNIVERSITY OF CHICAGO

Prepared for the Office of Nuclear Regulatory Research
U. S. NUCLEAR REGULATORY COMMISSION
under Interagency Agreement DOE 40-550-75

Argonne National Laboratory, with facilities in the states of Illinois and Idaho, is owned by the United States government, and operated by The University of Chicago under the provisions of a contract with the Department of Energy.

Available from

Superintendent of Documents
U. S. Government Printing Office
Post Office Box 37082
Washington, D.C. 20013-7982

and

National Technical Information Service
Springfield, VA 22161

NUREG/CR-3980 Vol. III
ANL-84-61 Vol. III

Distribution Code: R3

ARGONNE NATIONAL LABORATORY
9700 South Cass Avenue
Argonne, Illinois 60439

LIGHT-WATER-REACTOR SAFETY FUEL SYSTEMS RESEARCH PROGRAMS: QUARTERLY PROGRESS REPORT

July—September 1984

Date Published: April 1985

Previous reports in this series

ANL-83-85 Vol. III	July—September 1983
ANL-83-85 Vol. IV	October—December 1983
ANL-84-61 Vol. I	January—March 1984
ANL-84-61 Vol. II	April—June 1984

Prepared for the Division of Accident Evaluation
Office of Nuclear Regulatory Research
U. S. Nuclear Regulatory Commission
Washington, D. C. 20555
Under Interagency Agreement DOE 40-550-75

NRC FIN Nos. A2016 and A2017

LIGHT-WATER-REACTOR SAFETY
FUEL SYSTEMS RESEARCH PROGRAMS
QUARTERLY PROGRESS REPORT

July-September 1984

ABSTRACT

This progress report summarizes work performed by the Materials Science and Technology Division of Argonne National Laboratory during July, August, and September 1984 on water reactor safety problems related to fuel and cladding. The research and development areas covered are Transient Fuel Response and Fission Product Release and Clad Properties for Code Verification.

NRC Fin No.	FIN Title
A2016	Transient Fuel Response and Fission Product Release
A2017	Clad Properties for Code Verification

TABLE OF CONTENTS

LIGHT-WATER-REACTOR SAFETY
FUEL SYSTEMS RESEARCH PROGRAMS:
QUARTERLY PROGRESS REPORT

July-September 1984

EXECUTIVE SUMMARY

I. TRANSIENT FUEL RESPONSE AND FISSION PRODUCT RELEASE[a]

The validity of the FASTGRASS-VFP analysis of fission product behavior in solid fuel during the trace-irradiated SFD-ST experiment has been evaluated by comparing FASTGRASS-VFP against the more comprehensive GRASS-SST model. The results of this analysis show that, although FASTGRASS-VFP tends to overpredict intergranular bubble sizes as compared to GRASS-SST-calculated values for trace-irradiated fuel conditions, FASTGRASS-VFP predictions of fission product release rates for SFD-ST operating conditions appear to be reasonable. A more general edge-bubble interlinkage criterion than the one currently used in FASTGRASS-VFP is examined and implications for bubble interconnection in trace-irradiated fuel are discussed. Finally, the viability of rapid grain-boundary diffusion as a controlling mechanism for fission product release in trace-irradiated fuel is explored.

---

[a]RSR FIN Budget No. A2016; RSR Contact: L. Chan.

II. CLAD PROPERTIES FOR CODE VERIFICATION[b]

Zircaloy fuel cladding is susceptible to local breach-type failures during power transients in LWRs because of stresses imposed by differential thermal expansion of the fuel and cladding. In this program, the effect of stress state, strain rate, and temperature on the deformation characteristics of irradiated Zircaloy fuel cladding is being investigated to provide mechanical-property information and a failure criterion for the cladding under loading conditions conducive to pellet-cladding interaction (PCI). The information will be used in the development of codes to analyze PCI in fuel rods from power ramp experiments in test reactors, and to evaluate the susceptibility of extended-burnup fuel elements and new fuel element designs in commercial reactors to PCI failures during power transients.

In-reactor PCI is usually characterized by a highly localized stress and a mechanical constraint in the cladding produced as a result of the friction between the expanding pellet and cladding inner surface. The mechanical constraint is conducive to a plane-strain deformation condition of the highly anisotropic cladding. Under such a condition, the local cladding material is more susceptible to a low-ductility PCI failure. In this reporting period, fracture tests of H. B. Robinson spent-fuel cladding specimens in the modified expanding-mandrel apparatus continued. Two brittle-type failures were produced in specimens 217A4G and 217B2C. In the former specimen, evidence was obtained for propagation of a brittle crack at room temperature in a piece of cladding that contained incipient PCI-like cracks. The instantaneous propagation of the crack is inconsistent with a stress-corrosion cracking model but indicates a general embrittlement of the particular cladding specimen. The site of a through-wall crack of the 217B2C specimen has been located and SEM examination of fracture surface morphology is now in progress.

Several TEM specimens obtained from the 217A4G tube have been examined in this reporting period. No dislocations could be observed in the thin-foil specimens. This is consistent with the brittle crack propagation and with an extensive amount of pseudocleavage observed on the fracture surface that was

---

[b]RSR FIN Budget No. A2017; RSR Contact: H. H. Scott.

described in the previous quarterly report. Two types of general precipitates were observed in the 217A4G thin-foil specimens; one was cubic ZrO_2 and the other was zirconium hydride. By means of dark-field $2\frac{1}{2}$D-microscopy, both the cubic ZrO_2 and hydride precipitates were shown to be bulk phases. In contrast, the surficial nature of artifact χ-hydride and monoclinic-ZrO_2 phases could be clearly discerned by this technique. Although the role of the bulk hydride in the deformation and fracture behavior of the specimen at 325°C is not quite clear, it is evident that the general precipitation of the cubic ZrO_2 is associated with the brittle-type failure.

I. TRANSIENT FUEL RESPONSE AND FISSION PRODUCT RELEASE

Principal Investigator:
J. Rest

A. Validity of FASTGRASS-VFP Analysis of Fission Product Behavior in Solid Fuel During the Trace-irradiated SFD-ST Experiment

1. Formation of Intergranular Gas Bubbles During SFD-ST

A basic feature of FASTGRASS-VFP is that intergranular gas release is attributed to the development of a population of bubbles on grain edges and faces, and their subsequent linkup.[1] FASTGRASS-VFP has been used to interpret the trace-irradiated SFD-ST experiment performed in the PBF reactor in Idaho.[2,3] The largest grain-edge bubble predicted with FASTGRASS-VFP for the SFD-ST test is ~0.2 μm in diameter. However, micrographs of the SFD-ST tested fuel (Fig. 1.1) show reasonable evidence for the existence of bubbles ≥ 1 μm in diameter on the grain faces and edges.

The possibility that large bubbles can form on grain boundaries within 20 min is supported by observations made at Argonne by Gehl[4] on intergranular bubble growth in irradiated fuel during power-cooling-mismatch-type heating tests. Figure 1.2 shows posttest fractographs of fuel tested by a direct electrical heating (DEH) technique (left) and fuel tested in the PBF reactor. In the DEH-tested fuel, pretest intergranular bubble sizes were in the 10-50 nm range, while the posttest fractograph shown in Fig. 1.2 reveals bubbles ~0.2 μm in diameter. Bubbles ~0.2 μm in diameter were observed in fuel regions where the maximum temperature was ~2400 K (i.e., the same as the reported peak temperature in SFD-ST). When the bubbles reached 0.2 μm in diameter, continued bubble coalescence resulted in the formation of sinuous grain-surface channels, as seen in Fig. 1.2. Similar observations were made for the PBF-tested fuel. The transient time for these tests is on the order of minutes (e.g., the DEH test of the fuel shown in Fig. 1.2 lasted ~1 min).

Although the fuel used in these DEH and PBF experiments had a relatively high burnup, the observations made on the pre- and posttested

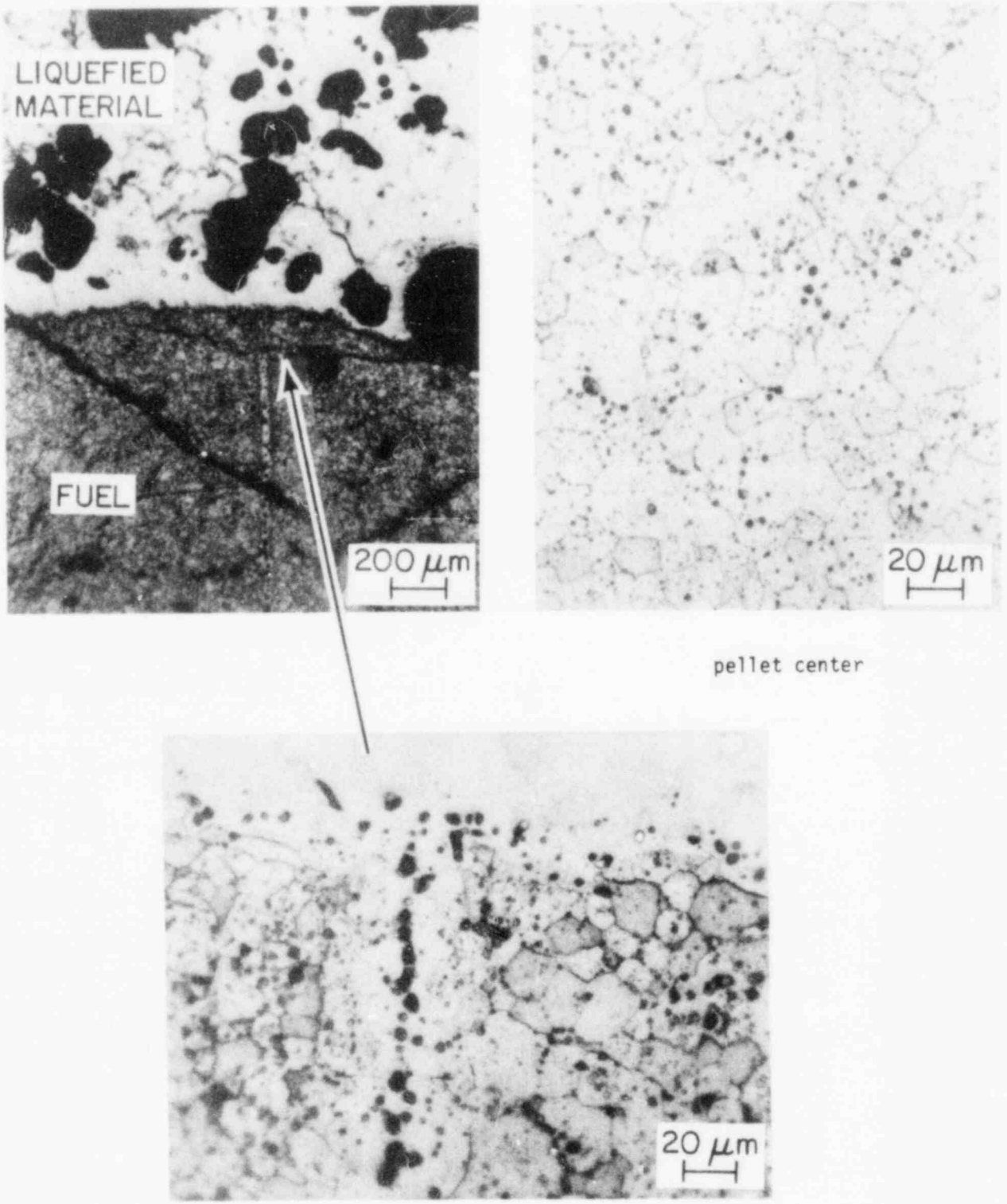

Fig. 1.1. Postirradiation Microstructure of the SFD-ST Fuel Remains, Indicating Grain Growth to 35 μm and UO_2 Oxidation to U_4O_9 Inclusions.

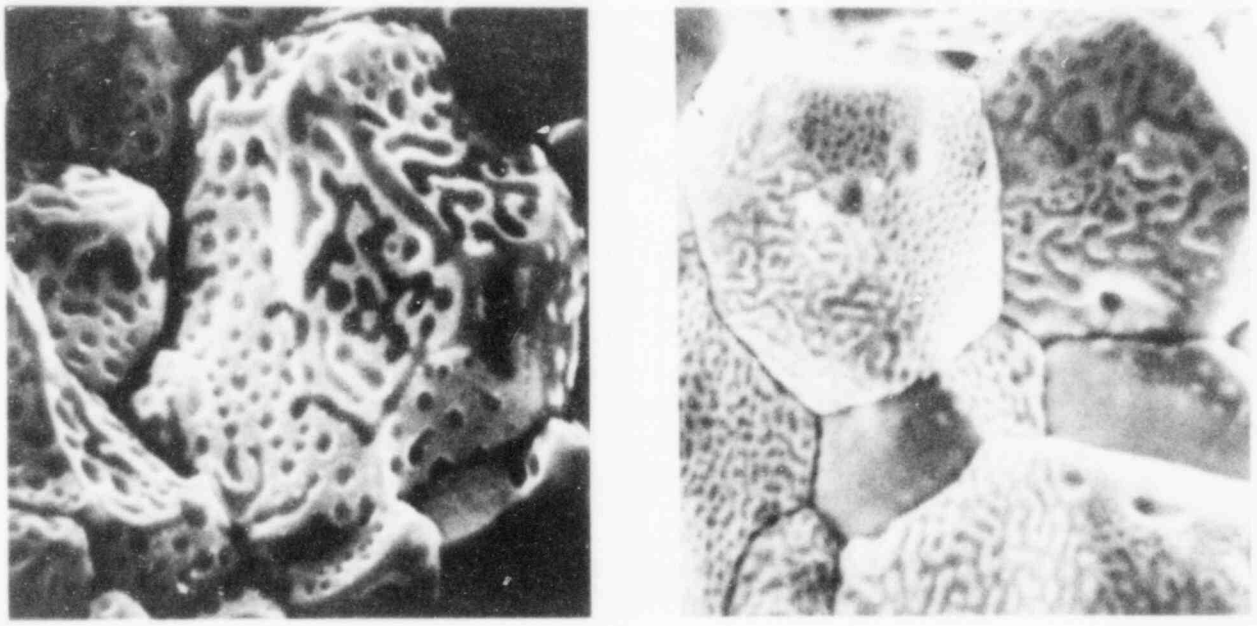

Fig. 1.2. Intergranular Bubbles as Revealed by Posttest Fuel Fractographs.

fuel indicate that rapid bubble growth is possible in relatively short time periods (i.e., extensive bubble growth can occur during a time period of 0.5-1 min). Thus, it appears plausible that intergranular bubble growth to sizes of ~0.2 μm diameter could have occurred during the SFD-ST test.

2. Comparison of FASTGRASS-VFP- and GRASS-SST-calculated Bubble Sizes

Given the validity of the above discussion, the next question one should ask concerns the accuracy and reliability of the FASTGRASS-VFP-calculated intergranular bubble sizes for SFD-ST conditions. The FASTGRASS-VFP model was developed to satisfy the need for a fast-running alternative to the much more detailed GRASS-SST code.[5] The most important differences between FASTGRASS-VFP and GRASS-SST are in the methods used for calculating the evolution of bubble density and size over time. In GRASS-SST, the bubble size distribution is specified by calculating the densities of bubbles in each of a number of bubble size classes. Each bubble size class is characterized by an average number of atoms per bubble, the value of which differs from that of the preceding size class by a constant multi-

plier. (The number of size cla ;es is a variable that is determined dynamically during the calculation.) Changes in the bubble size distribution, caused by bubble coalescence and re-solution, for example, are determined by solving a relatively large number of coupled nonlinear differential equations for each time step. Solutions are carried out for bubbles on grain faces and edges, along dislocations, and in the bulk matrix. The iterative solution of a large number of coupled equations within this rate theory approach contributes significantly to the computer run times of GRASS-SST.

In contrast to the multiclass description of the bubble size distribution in GRASS-SST, FASTGRASS-VFP uses only one bubble size class. Whereas the behavior of fission gas bubbles at the grain face and grain edge in FASTGRASS-VFP is based entirely on this single size-class description, the description of intragranular fission-gas behavior includes the kinetics of fission-gas-atom generation and migration and fission-gas-bubble/gas-atom interactions. The intragranular single gas atoms are characterized by number density; the intragranular, grain-face, and grain-edge bubbles are characterized by number density and the average number of atoms per bubble, $S_i(t)$. (The index i refers to a particular intra- or intergranular bubble.)

The approach to modeling the evolution of the number of atoms per bubble, $S_i(t)$, in FASTGRASS-VFP is based on a numerical algorithm which compares the overall bubble growth and shrinkage rates and, on the basis of the results, increases or decreases $S_i(t)$ by a factor close to 1. This method of solution for $S_i(t)$ was chosen in order to obtain the required degree of FASTGRASS-VFP execution efficiency. As this method is somewhat arbitrary, although its basis is physically reasonable, it must be benchmarked against the comprehensive bubble-size distribution calculations in GRASS-SST.

Although this type of benchmarking has been performed frequently in the past, it has never been attemped for trace-irradiated fuel. A comparison of GRASS-SST- and FASTGRASS-VFP-calculated bubble sizes has been made for the SFD-ST experiment and is presented below.

Figures 1.3-1.5 show a comparison between the GRASS-SST-calculated grain-edge bubble size distribution and the FASTGRASS-VFP-calculated average grain-edge bubble size for SFD-ST (prior to the requench, and not including fuel liquefaction) for three values of the fuel temperature: 1942 K (Fig. 1.3), 2193 K (Fig. 1.4), and 2400 K (Fig. 1.5). The axial fuel temperature profiles for SFD-ST (e.g., see Fig. 1.6) were used in the GRASS-SST and FASTGRASS-VFP simulations. This was accomplished by subdividing the fuel into 6 axial regions. The results shown in Figs. 1.3-1.5 are for the region of peak fuel temperature at three successive transient times.

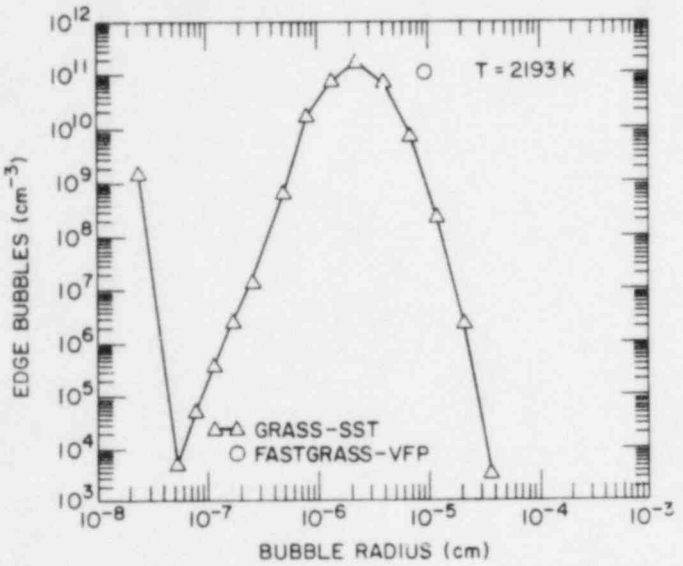

Fig. 1.3

Comparison Between GRASS-SST-calculated Edge-Bubble Size Distribution and FASTGRASS-VFP-calculated Average Edge-Bubble Size for SFD-ST at 1942 K.

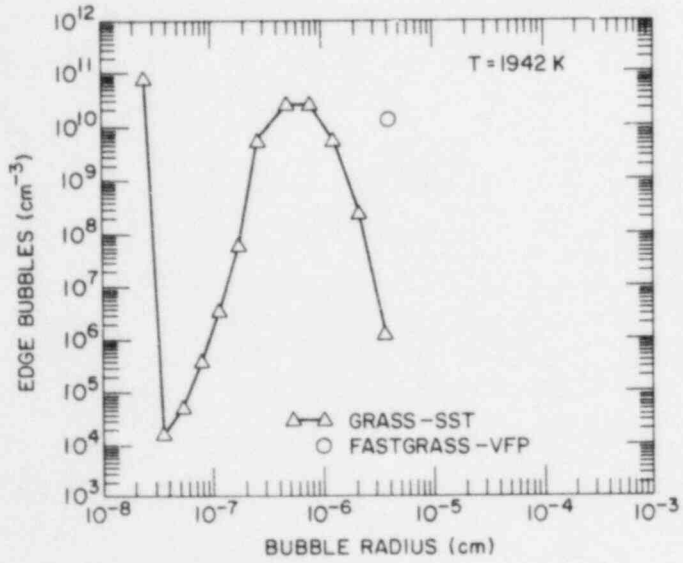

Fig. 1.4

Comparison Between GRASS-SST-calculated Edge-Bubble Size Distribution and FASTGRASS-VFP-calculated Average Edge-Bubble Size for SFD-ST at 2193 K.

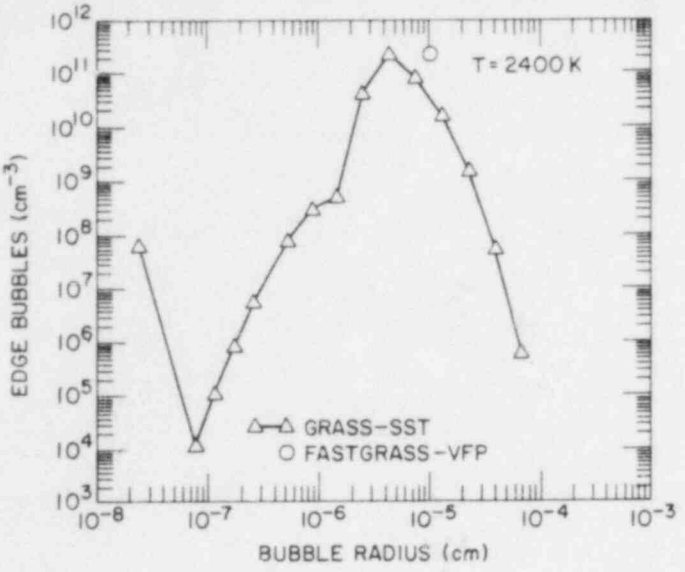

Fig. 1.5

Comparison Between GRASS-SST-calculated Edge-Bubble Size Distribution and FASTGRASS-VFP-calculated Average Edge-Bubble Size for SFD-ST at 2400 K.

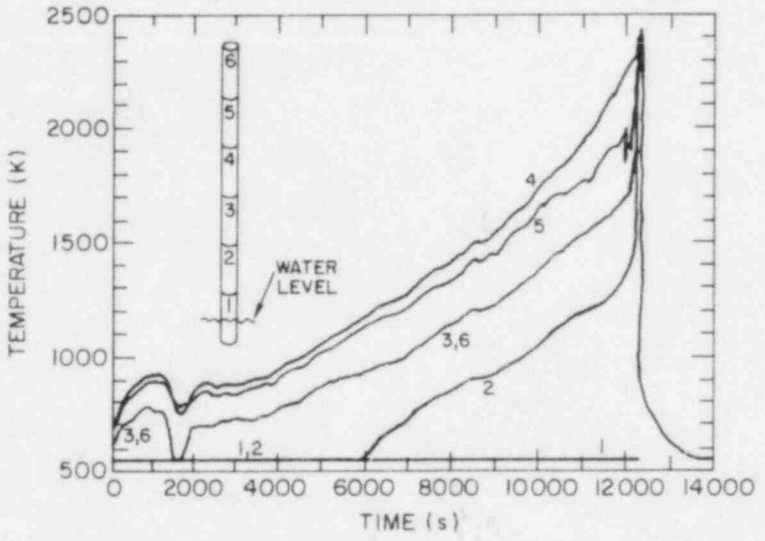

Fig. 1.6. Temperature Profiles for Axial Fuel Rod Sections 1 to 6 (See Inset) in the SFD-ST Experiment.

Figures 1.3-1.5 show that for SFD-ST (trace-irradiated) conditions, the average bubble radius predicted by FASTGRASS-VFP is larger than the peak radius in the GRASS-SST grain-edge bubble-size distribution, but that the difference becomes smaller as the fuel temperature increases. For example, at 1942 K, FASTGRASS-VFP predicts an average bubble radius that is about a factor of 10 larger than the position of the peak of the GRASS-SST-calculated bubble-size distribution, whereas at 2400 K this difference is only about a factor of 2. The corresponding results for the grain-face bubbles are shown in Figs. 1.7-1.9. The relationship between the GRASS-SST-

and FASTGRASS-VFP-calculated grain-face bubble sizes is similar to that observed for the grain-edge bubble sizes.

Both GRASS-SST and FASTGRASS-VFP predict the absence of intragranular bubbles for SFD-ST in this temperature range (i.e., prior to fuel liquefaction and the requench). In addition, GRASS-SST predicts that 99.99% of the intergranular gas is in bubbles; this prediction supports the assumption made in FASTGRASS-VFP that only average bubble sizes are required to characterize the intergranular bubble-size distributions.

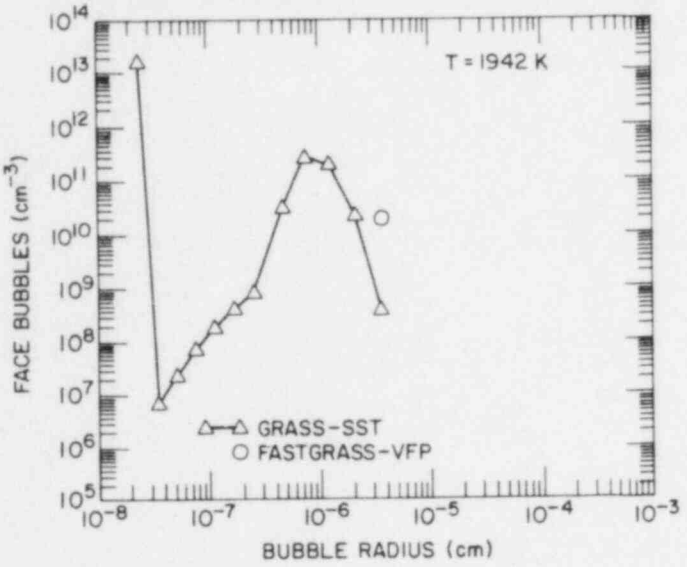

Fig. 1.7

Comparison Between GRASS-SST-calculated Face-Bubble Size Distribution and FASTGRASS-VFP-calculated Average Face-Bubble Size for SFD-ST at 1942 K.

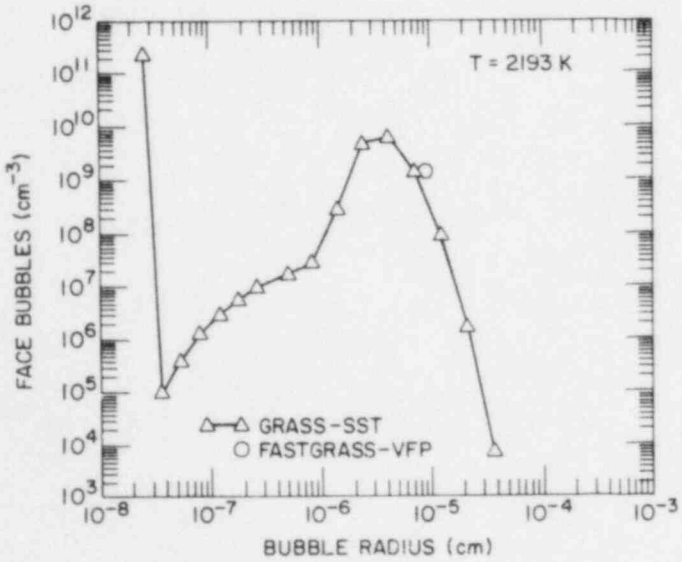

Fig. 1.8

Comparison Between GRASS-SST-calculated Face-Bubble Size Distribution and FASTGRASS-VFP-calculated Average Face-Bubble Size for SFD-ST at 2193 K.

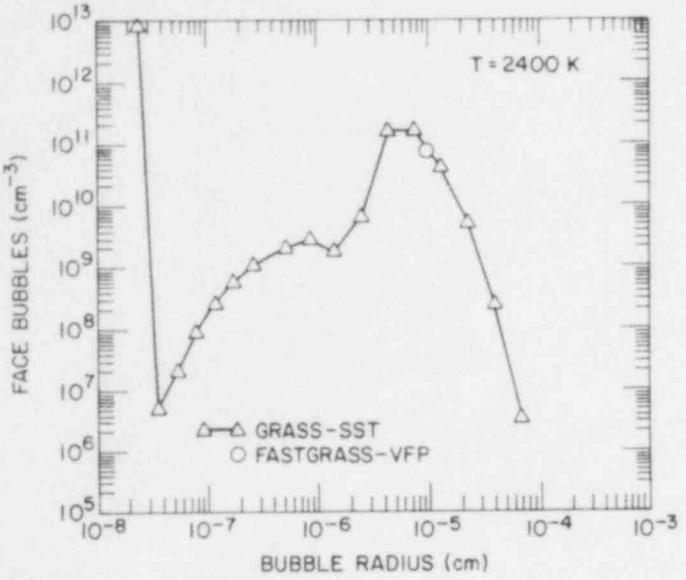

Fig. 1.9

Comparison Between GRASS-SST-calculated Face-Bubble Size Distribution and FASTGRASS-VFP-calculated Average Face-Bubble Size for SFD-ST at 2400 K.

Figures 1.10 and 1.11 show GRASS-SST-calculated grain-edge and grain-face bubble size distributions, respectively, for peak fuel temperatures of 1942, 2193, and 2400 K. For both grain-edge and grain-face bubbles, the peak of the bubble size distribution is predicted to occur at larger bubble sizes with increased fuel temperature. The FASTGRASS-VFP results are in agreement with this conclusion (i.e., see Figs. 1.3-1.5 and 1.7-1.9).

In order to compare FASTGRASS-VFP-calculated average bubble size with the peak in the GRASS-SST-calculated bubble size distribution for burnup conditions other than trace-irradiated, calculations were performed for an SFD-ST-type transient (prior to requench and without fuel liquefaction) on fuel that was previously irradiated (at the same temperatures as the SFD-ST preconditioning) to a peak burnup of ~4.0 at.%. The results of this calculation are shown in Fig. 1.12 for grain-edge bubbles, and in Figs. 1.13-1.15 for grain-face bubbles. Figure 1.12 and Figs. 1.13-1.15 are analogous to Fig. 1.3 and Figs. 1.7-1.9, respectively. FASTGRASS-VFP and GRASS-SST calculations for grain-edge bubbles are shown at a fuel temperature of 1942 K only (Fig. 1.12), as both codes predict negligible gas content on the grain edges at higher fuel temperatures owing to extensive edge-porosity interlinkage and subsequent gas release.

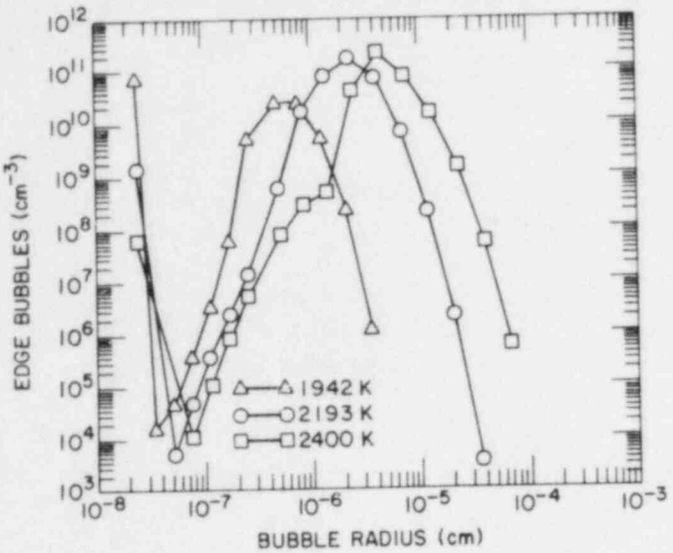

Fig. 1.10

GRASS-SST-calculated Edge-Bubble Size Distributions for SFD-ST at Three Values of the Peak Fuel Temperature.

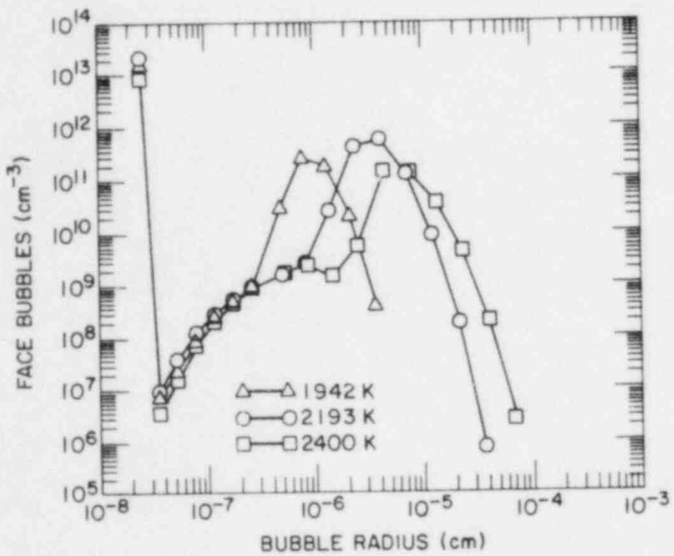

Fig. 1.11

GRASS-SST-calculated Face-Bubble Size Distributions for SFD-ST at Three Values of the Peak Fuel Temperature.

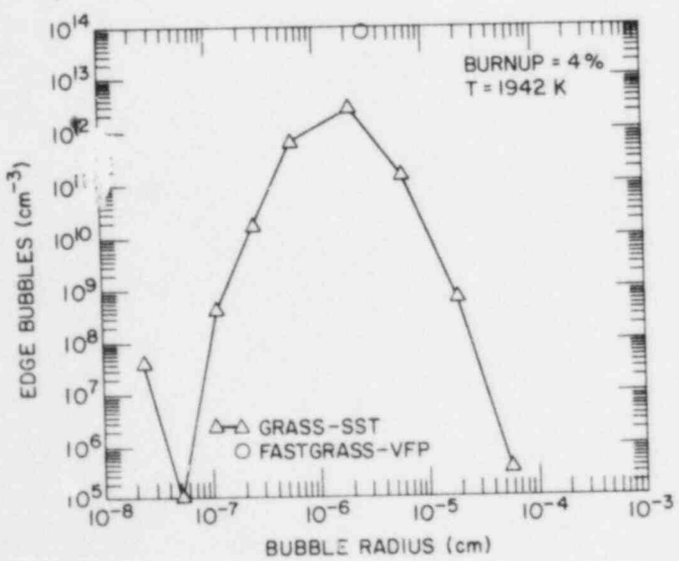

Fig. 1.12

Comparison Between GRASS-SST-Calculated Edge-Bubble Size Distribution and FASTGRASS-VFP-calculated Average Edge-Bubble Size at 1942 K for SFD-ST-Type Transient on Fuel Irradiated to a Peak Burnup of ~4 at.%.

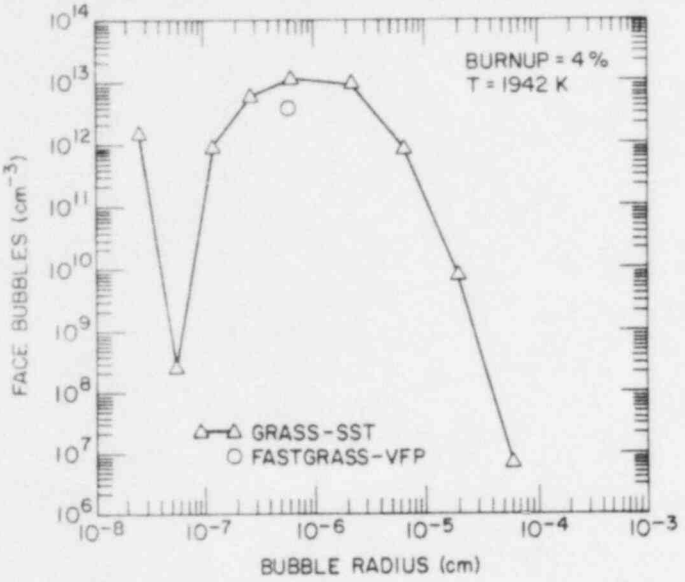

Fig. 1.13

Comparison Between GRASS-SST-calculated Face-Bubble Size Distribution and FASTGRASS-VFP-calculated Average Face-Bubble Size at 1942 K for SFD-ST-Type Transient on Fuel Irradiated to a Peak Burnup of ~4 at.%.

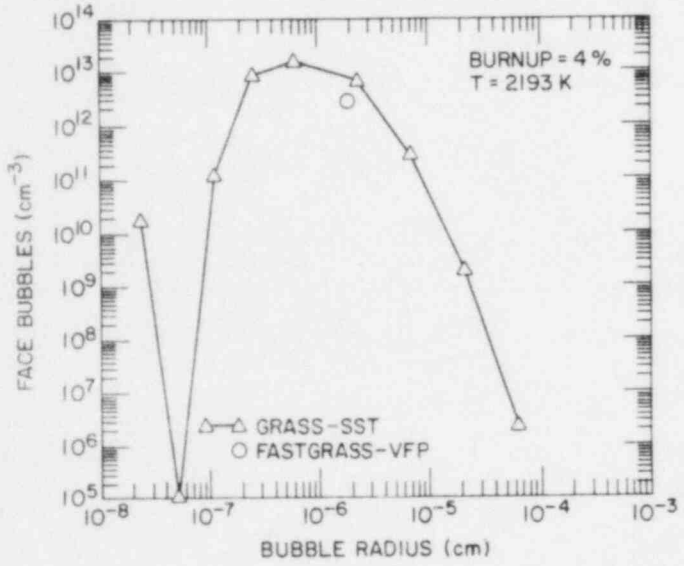

Fig. 1.14

Comparison Between GRASS-SST-calculated Face-Bubble Size Distribution and FASTGRASS-VFP-calculated Average Face-Bubble Size at 2193 K for SFD-ST-Type Transient on Fuel Irradiated to a Peak Burnup of ~4 at.%.

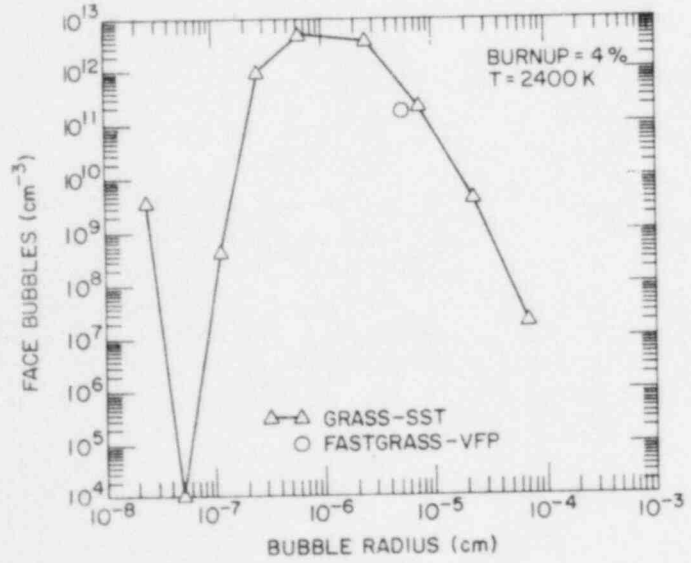

Fig. 1.15

Comparison Between GRASS-SST-calculated Face-Bubble Size Distribution and FASTGRASS-VFP-calculated Average Face-Bubble Size at 2400 K for SFD-ST-Type Transient on Fuel Irradiated to a Peak Burnup of ~4 at.%.

Figures 1.12-1.15 demonstrate that for this value of fuel burnup (~4.0 at.%), FASTGRASS-VFP is reasonably accurate in predicting the position of the peak of the GRASS-SST-calculated intergranular bubble-size distribution. The greatest discrepancy between FASTGRASS-VFP and GRASS-SST occurs at 2400 K, where an average grain-face bubble size about a factor of three larger than the position of the peak of the face-bubble size distribution is predicted (Fig. 1.15). At 1942 K, FASTGRASS-VFP calculates average intergranular bubble sizes almost coincident with the position of the peaks of the calculated intergranular bubble-size distributions (Figs. 1.12 and 1.13). In Fig. 1.12, the FASTGRASS-VFP-predicted density of the average-size grain-edge bubble is about 1 1/2 orders of magnitude larger than the peak value in the GRASS-SST calculated density. However, this is reasonable in that FASTGRASS-VFP is putting all the gas into bubbles that have an average size equal to the size of a bubble at the peak of the bubble-size distribution. Thus, the density of these average-size bubbles should be higher than the peak of the distribution for a given quantity of gas.

The relatively good agreement between FASTGRASS-VFP- and GRASS-SST-calculated bubble sizes shown in Figs. 1.12-1.15 is not restricted to the high burnup value that was used (i.e., 4.0 at.%). In fact, the axial distribution of burnup for this irradiation simulation ranged from 1.36 to 4.07 at.%. Previous work has demonstrated that FASTGRASS-VFP has the capability to provide a reasonable estimate of the position of the peak in the GRASS-SST-calculated bubble size distribution for fuel burnups between 0.1 and 12 at.% (i.e., within the range of burnups examined thus far). A peak fuel burnup of ~4.0 at.% was selected for the analysis described in this report because of the current interest in the SFD 1-3 and SFD 1-4 experiments, for which the peak fuel burnup is close to this value.

3. Comparison of Two Different Edge-Porosity Interlinkage Criteria

The pore-interlinkage model used in both FASTGRASS-VFP and GRASS-SST is based on observations of Turnbull and Tucker,[6] who reported that a stabilized network of interconnected porosity is established when the grain-edge bubble swelling strain reaches ~5%. To account for local fluctuations in fuel microstructure and gas bubble morphology, the grain-edge porosity

interlinkage fraction, PRF, is assumed to be a statistical distribution around an average value of the grain-edge swelling, B_{vedge}:

$$PRF = \frac{1}{\sigma_E\sqrt{2\pi}} \int_{x=B_{vcrit}}^{\infty} \exp\left[-\left(x - B_{vedge}\right)^2/2\sigma_E^2\right]dx. \qquad (1.1)$$

The width of the distribution, σ_E, is a function of variations in structural parameters, depending on the local fuel condition and heterogeneity, and can in principle be determined experimentally; $B_{vcrit} = 0.05$ is the value of grain-edge swelling at which long-range interconnection would take place if the fuel microstructure and gas-bubble morphology were homogeneous. In implementing Eq. (1.1) into GRASS-SST and FASTGRASS-VFP, the edge tunnels are allowed to pinch off after gas release occurs; i.e., PRF in Eq. (1.1) will decrease. Subsequently, as additional gas arrives at the grain edges, PRF will again increase, simulating the opening and closing of grain-edge porosity.

However, as pointed out by D. Olander,[7] in the FASTGRASS-VFP simulation of the SFD-ST test, given the calculated grain-edge average bubble size RD(4) and density Y(4), grain-edge bubble interconnection is predicted to occur at a fuel temperature of ~2200 K by bubble-bubble contact for values of grain-edge bubble swelling below 1%. It is important to note that this prediction is for the peak temperature node only.

In order to investigate these ideas further, the interconnection criterion of Eq. (1.1), based on grain-edge bubble swelling, was replaced with one based on bubble-bubble contact. Assuming a tetrakaidecahedral geometry, the edge-bubble length per grain-edge length, E_{LINK}, can be expressed as

$$E_{LINK} = \frac{Y(4)\left(\frac{\text{bubbles}}{\text{cm}^3}\right)2RD(4)\left(\frac{\text{bubble length}}{\text{bubble}}\right)\frac{\pi}{6}d^3\left(\frac{\text{cm}^3}{\text{grain}}\right)\frac{1}{12}\left(\frac{\text{grains}}{\text{edge}}\right)}{(\pi/48\sqrt{2})^{1/3}\,d(\text{edge length})}$$

$$= Y(4)\cdot RD(4)\cdot d^2/4.11,$$

where d is the grain diameter.

When $E_{LINK} \geq 1.0$, grain-edge bubble interlinkage is predicted to occur. In order to account for local fluctuations in fuel microstructure and gas-bubble morphology, the bubble interlinkage probability is assumed, in analogy with the treatment leading to Eq. (1.1), to be a statistical distribution around an average value of E_{LINK}:

$$PRF = \frac{1}{\sigma_L \sqrt{2\pi}} \int_{x=1.0}^{\infty} \exp\left[- x\left(- E_{LINK}\right)^2 / 2\sigma_L^2 \right] dx. \qquad (1.2)$$

Again, as in Eq. (1.1), PRF will decrease after gas release occurs, simulating the opening and closing of grain-edge porosity.

Figure 1.16 shows FASTGRASS-VFP predictions of the fractional fission-gas release rate for SFD-ST as a function of the peak fuel temperature. One curve represents calculations based on Eq. (1.1). The other two curves represent calculations based on the bubble-bubble contact criterion of Eq. (1.2), with σ_L = 0.1 and 0.6, respectively. The value for σ_L of 0.6 is in the same ratio to the "critical" value of E_{LINK} (i.e., 1.0) as the value (0.03) for σ_E in Eq. (1.1) is to the critical value of edge-bubble swelling (0.05).

The results in Fig. 1.16 show that the predictions made with the bubble-bubble contact criterion of Eq. (1.2) for the two values of σ_L bound the predictions made with the grain-edge bubble swelling criterion of Eq. (1.1). Thus, it appears that the extrapolation of Eq. (1.1) to trace-irradiated fuel conditions is not totally unreasonable. A more realistic interlinkage criterion would be to use Eq. (1.2), allowing the edge tunnels to pinch off after gas release occurs for values of edge-bubble swelling less than B_{vcrit}; for values of edge-bubble swelling greater than B_{vcrit}, the grain-edge porosity would remain open and stable. Of course, the validity of these ideas depends on the assumption that the transient edge-tunnel kinetics are somewhat similar to the kinetics observed by Turnbull and Tucker under steady-state irradiation conditions. The truth of this assumption is certainly not obvious.

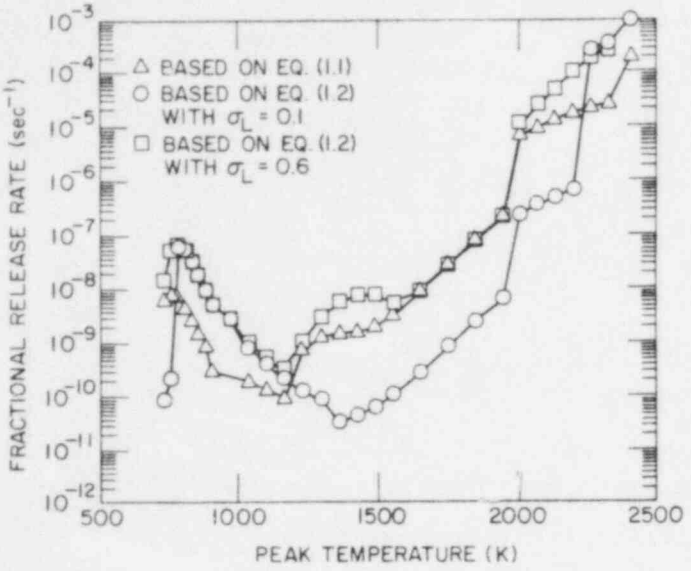

Fig. 1.16

Comparison of FASTGRASS-VFP Predictions of Fractional Fission-Gas Release Rate during SFD-ST for Two Different Edge-Bubble Interlinkage Criteria.

4. Is Rapid Grain-Boundary Diffusion a Viable Mechanism of Fission Gas Release During SFD-ST?

Figure 1.17 compares the results of FASTGRASS-VFP and GRASS-SST calculations of fractional fission gas release rate vs. peak fuel temperature for SFD-ST. FASTGRASS-VFP calculates a much higher fractional release rate than GRASS-SST for peak fuel temperatures below ~1600 K. In both cases, the total fractional releases calculated are very small in this peak-temperature range (2×10^{-3}%; see Fig. 1.18). One might speculate that a mechanism of fission gas release not included in either code is responsible for the discrepancy between the calculated and measured quantities (i.e., GRASS-SST underpredicts the data for peak fuel temperatures below 1600 K, whereas FASTGRASS-VFP results are in better agreement with the data for peak fuel temperatures between 1000 and 2400 K; see Figs. 1.17 and 1.19).

Recently, Prustin et al.[8] have suggested that rapid grain-boundary diffusion of fission gas atoms might be the controlling mechanism for fission gas release in trace-irradiated fuel. This mechanism of fission gas release (i.e., diffusion along the grain boundaries over macroscopic distances to the fuel surface) is not currently included in FASTGRASS-VFP. In order to assess the viability of rapid grain-boundary diffusion of fission gas atoms as a potential mechanism underlying the SFD-ST release behavior at temperatures below 1600 K, calculations for grain boundary diffusion

in a slab based on the analysis of J. C. Fisher[9] were performed. These calculations assume a uniform, constant concentration, C_g, of gas atoms at one face of the slab (y = 0), a grain boundary of width 10^{-7} cm (in the x direction), infinite extension in the z direction, and diffusion in both the bulk and on the boundary in the +y direction. In addition, it is assumed that the gas-atom diffusivity is greater on the boundary than in the lattice, and the ratio of the two diffusivities (D_g/D_l) is input to the calculations. In performing these calculations, reported values[8] for the intragranular gas-atom diffusion coefficient (10^{-13} cm^2/s at 1400°C) and activation energy (1.3×10^5 cal) were used to estimate the diffusivity of the gas atoms in the fuel matrix.

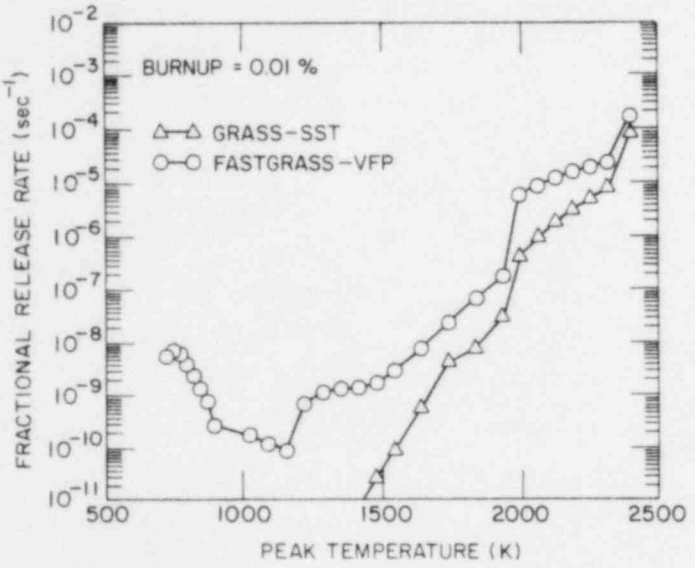

Fig. 1.17

Comparison Between FASTGRASS-VFP and GRASS-SST Calculations of Fractional Fission-Gas Release Rate vs. Peak Temperature for SFD-ST.

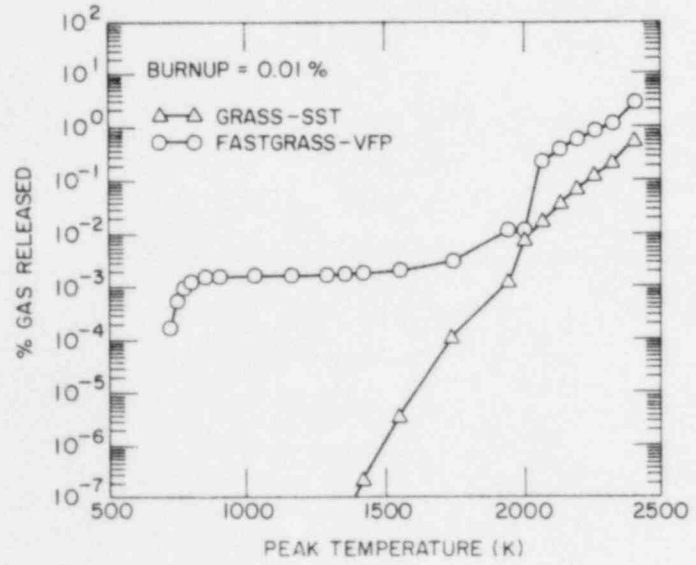

Fig. 1.18

Comparison Between FASTGRASS-VFP and GRASS-SST Calculations of Fractional Fission-Gas Release vs. Peak Fuel Temperature for SFD-ST.

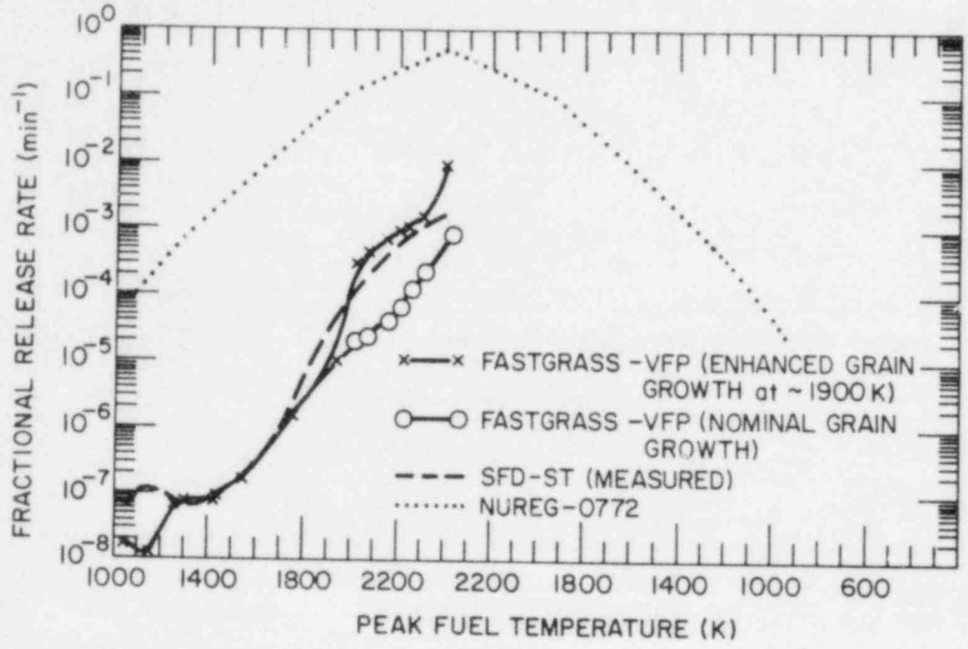

Fig. 1.19. Comparison Between FASTGRASS-VFP-calculated and Measured Values of Fission-Gas Release Rate for SFD-ST.

Table 1.1 shows the calculated fractional concentrations, C/C_g, of the diffusing species as a function of y/L (where L = fuel radius) at the end of a 20-min period at 2200 K for three values of D_g/D_l. The value of L was taken as 0.42 cm (i.e., the radius of the SFD-ST fuel). The second and third columns of results in Table 1.1 correspond to diffusion distances of 1 and 10 grain diameters, respectively. The results in Table 1.1 indicate that for ratios of $D_g/D_l > 10^6$, rapid grain-boundary diffusion from fuel

TABLE 1.1.

C/C_g as a Function of y/L (L = 0.42 cm) after 20 min at 2200 K

	y/L					
D_g/D_l	0.0	2.38×10^{-3}	2.38×10^{-2}	0.25	0.5	1.0
10	1.0	4.51×10^{-14}	0	0.0	0.0	0.0
10^4	1.0	0.38	5.98×10^{-5}	0.0	0.0	0.0
10^6	1.0	0.91	0.38	3.68×10^{-5}	4.97×10^{-14}	0.0

having an effective radius of 0.25L will result in fractional gas release on the order of 4×10^{-3}% after 20 min at 2200 K.

If rapid grain-boundary diffusion of fission gas is to occur at these temperatures (i.e., after 20 min at 2200 K, as shown in Table 1.1), then the majority of the fission gas on the grain faces must be in atomic form (i.e., not in bubbles). Figure 1.20 shows the GRASS-SST-calculated fraction of grain-face gas in bubbles vs. fuel temperature for SFD-ST. At temperatures above 1900 K, the majority of grain-face gas is predicted to be in gas bubbles. Thus, rapid grain-boundary diffusion of gas atoms at temperatures above 1900 K does not appear to be a viable mechanism of fission gas release for SFD-ST accident conditions.

For fuel temperatures below 2200 K, C/C_g values for $D_g/D_l = 10^6$ decrease in an exponential fashion. For example, after 20 min at 1600 K, the fractional concentration for the set of y/L vs. D_g/D_l values listed in Table 1.1 is about 2×10^{-2} at a distance of one grain diameter and zero everywhere else. Thus, these results suggest that rapid grain-boundary diffusion alone is not sufficient to explain the SFD-ST release behavior at temperatures below 1600 K.

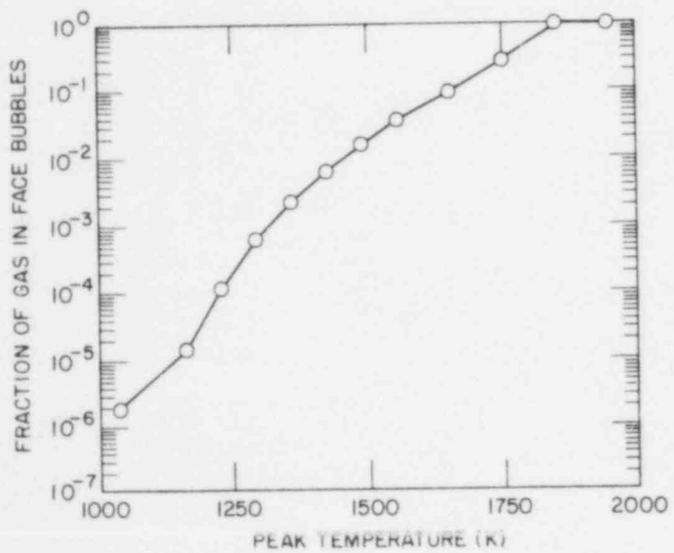

Fig. 1.20

GRASS-SST-calculated Fraction of Grain-Face Gas in Bubbles vs. Peak Fuel Temperature for SFD-ST.

B. References for Chapter I

1. J. Rest, An Improved Model for Fission Product Behavior in Nuclear Fuel Under Normal and Accident Conditions, J. Nucl. Mater. 120 (2&3), 195-212 (1984).

2. J. Rest, "The Mechanistic Prediction of Fission Gas, Iodine, and Cesium Release From LWR Fuel Under Degraded-Core Accident Conditions," to be published in the Proceedings of the ANS Topical Meeting on Fission Product Behavior and Source Term Research, Snowbird, UT, July 15-19, 1984.

3. J. Rest, The Coupled Kinetics of Grain Growth and Fission Product Behavior in Nuclear Fuel Under Degraded-Core Accident Conditions, to be published in J. Nucl. Mater.

4. S. M. Gehl, The Release of Fission Gas During Transient Heating of LWR Fuel, NUREG/CR-2777, ANL-80-108 (May 1982).

5. J. Rest, GRASS-SST: A Comprehensive, Mechanistic Model for the Prediction of Fission-Gas Behavior in UO_2-Base Fuels During Steady-State and Transient Conditions, NUREG/CR-0202, ANL-78-53 (June 1978).

6. J. A. Turnbull and M. O. Tucker, Swelling in UO_2 Under Conditions of Gas Release, Philos. Mag. 30, 47 (1972).

7. D. Olander, private communication (1984).

8. S. G. Prussin, D. R. Olander, P. Goubeault, and D. Bayen, "Release of Volatile Fission Products From UO_2," to be published in the Proceedings of the ANS Topical Meeting on Fission Product Behavior and Source Term Research, Snowbird, UT, July 15-19, 1984.

9. J. C. Fisher, Calculation of Diffusion Penetration Curves for Surface and Grain Boundary Diffusion, J. Appl. Phys. 22, 74-77 (1951).

II. CLAD PROPERTIES FOR CODE VERIFICATION

Principal Investigators:
H. M. Chung, F. L. Yaggee, and T. F. Kassner

The Zircaloy cladding of fuel rods in light-water-cooled reactors is susceptible to local breach-type failures, commonly known as pellet-cladding interaction (PCI) failures, during power transients after the fuel has achieved sufficiently high burnup. As a result of the high burnup, the gap between the UO_2 fuel pellets and the cladding is closed and highly localized stress is believed to be imposed on the cladding during power transients by differential thermal expansion of the cracked fuel and cladding. In addition to the localized stress, a high-burnup fuel cladding is also characterized by high-density radiation-induced defects, mechanical constraints imposed by pellet-cladding friction, compositional changes (e.g., oxygen and hydrogen uptake associated with in-service corrosion), and geometrical changes due to creep-down and bowing. It is possible that synergistic effects involving more than one of the above factors influence the deformation and fracture of the in-reactor fuel cladding, e.g., strain aging associated with impurity or alloying elements, irradiation- or stress-induced segregation of the elements, and subsequent formation of nonequilibrium phases. Although mechanisms of stress corrosion cracking associated with volatile fission products such as I and liquid metal embrittlement associated with an element such as Cd have been well established for local breach-type failures of irradiated and unirradiated Zircaloy cladding under out-of-reactor simulation conditions, conclusive evidence of these processes is not yet available for in-reactor PCI failures. Consequently, to provide a better understanding of the PCI phenomenon, we have undertaken a mechanistic study of the deformation and fracture behavior of actual power-reactor fuel cladding discharged after a high burnup.

In this program, the effect of temperature, strain rate, and stress localization on the deformation and fracture characteristics of Zircaloy cladding from spent-fuel rods is being investigated by means of internal gas-pressurization and mandrel-loading experiments in the absence of simulated fission product species. The deformed and fractured specimens of spent-fuel

cladding are then being examined by optical microscopy, scanning electron microscopy (SEM), transmission electron microscopy (TEM), and high-voltage electron microscopy (HVEM). The results of microstructural and fracture-property investigations will be used to develop a failure criterion for the cladding under PCI-type loading conditions. The information will be incorporated into fuel performance codes, which can be used to evaluate the susceptibility of extended-burnup fuel elements in commercial reactors to PCI failures during power transients in later cycles, and to evaluate cladding performance and reliability of new fuel-element designs. An optimization of power ramp procedures to minimize cladding failures would result in a significant decrease in radiation exposure of plant personnel due to background and airborne radioactivity as well as an extension of core life in terms of allowable off-gas radioactivity.

A. TEM Characterization of H. B. Robinson Cladding Fractured by Modified Expanding-Mandrel Loading (H. M. Chung)

1. Introduction

The fracture behavior and fracture surface morphologies of the H. B. Robinson cladding specimen 217A4G have been reported previously.[1] The specimen failed in a brittle manner after loading at 325°C with the modified expanding-mandrel apparatus. In this reporting period, several thin-foil specimens obtained from regions adjacent to the failure site (see Fig. 2.1 of Ref. 1) of the 217A4G tube were prepared and examined by TEM and HVEM.

2. TEM Microstructural Characteristics of Brittle-Type Failure Specimen 217A4G

A general TEM examination of several thin-foil specimens was conducted. It was immediately noticeable that few dislocations could be observed in the specimens. This is consistent with the extensive amount of pseudocleavage feature observed in the fracture surface of the 217A4G tube.[1] Because of the difficulty in obtaining regions that contained dislocations, an analysis of Zr_3O diffraction characteristics similar to those reported previously for specimens 165AE4A[1] and 165AE4B could not be conducted.

The most noticeable microstructural characteristics of the 217A4G specimen were the presence of general precipitates of previously unidentified phases, as shown in Fig. 2.1. The bright-field image of Fig. 2.1(A) indicates two types of precipitates, denoted by arrows C and γ, respectively. The selected-area diffraction (SAD) pattern is indexed in Fig. 2.1(B). Besides the α-Zr matrix reflections [zone axis $(5\bar{1}\bar{4}\bar{9})_\alpha$], reflections associated with three other phases were identified in the SAD pattern, i.e., cubic ZrO_2, a bulk phase of zirconium hydride (δ- or γ-hydride), and an artifact surface χ-hydride.

The cubic ZrO_2 has a fluorite structure[2] with an fcc unit cell of lattice constant a_o = 0.5135 nm. One unit cell contains 4 Zr atoms at (000), $(\frac{1}{2}\ 0\ \frac{1}{2})$, $(0\ \frac{1}{2}\ \frac{1}{2})$, and $(\frac{1}{2}\ \frac{1}{2}\ 0)$, and 8 oxygen atoms at $(\frac{1}{4}\ \frac{1}{4}\ \frac{1}{4})$, $(\frac{1}{4}\ \frac{3}{4}\ \frac{1}{4})$, $(\frac{3}{4}\ \frac{1}{4}\ \frac{1}{4})$, $(\frac{3}{4}\ \frac{3}{4}\ \frac{1}{4})$, $(\frac{1}{4}\ \frac{1}{4}\ \frac{3}{4})$, $(\frac{1}{4}\ \frac{3}{4}\ \frac{3}{4})$, $(\frac{3}{4}\ \frac{1}{4}\ \frac{3}{4})$, and $(\frac{3}{4}\ \frac{3}{4}\ \frac{3}{4})$. Structure factor calculation shows no superlattice reflections. The calculated interplanar spacings of the cubic-ZrO_2 phase are summarized in Table 2.1.

The structure of the artifact χ-hydride is tetragonal with lattice constants a_o = 0.522 nm and c_o = 0.514 nm. The surficial nature of the hydride has been reported elsewhere.[3] The interplanar spacings of the χ-hydride are summarized in Table 2.2.

Inspection of Tables 2.1 and 2.2 shows that for each cubic-ZrO_2 reflection, there exists a similar reflection of the χ-hydride with a similar interplanar spacing. Therefore, in practice, it is difficult to separate the reflections from the cubic ZrO_2 and the primary reflections from the χ-hydride. However, the distinct superlattice reflections of the χ-hydride provide a convenient clue as to the presence of the phase.

The structures of γ- and δ-hydrides of zirconium have been reported by Sidhu et al.[4] The γ-hydride is an ordered fct phase (a_o = 0.460 nm and c_o = 0.497 nm), with hydrogen atoms occupying the tetrahedral interstices at $(\frac{1}{4}\ \frac{1}{4}\ \frac{1}{4})$, $(\frac{1}{4}\ \frac{1}{4}\ \frac{3}{4})$, $(\frac{3}{4}\ \frac{3}{4}\ \frac{1}{4})$, and $(\frac{3}{4}\ \frac{3}{4}\ \frac{3}{4})$. It has approximately the chemical composition of ZrH. As the number of hydrogen atoms in the unit cell increases, the intensity of the superlattice reflections of the γ-hydride

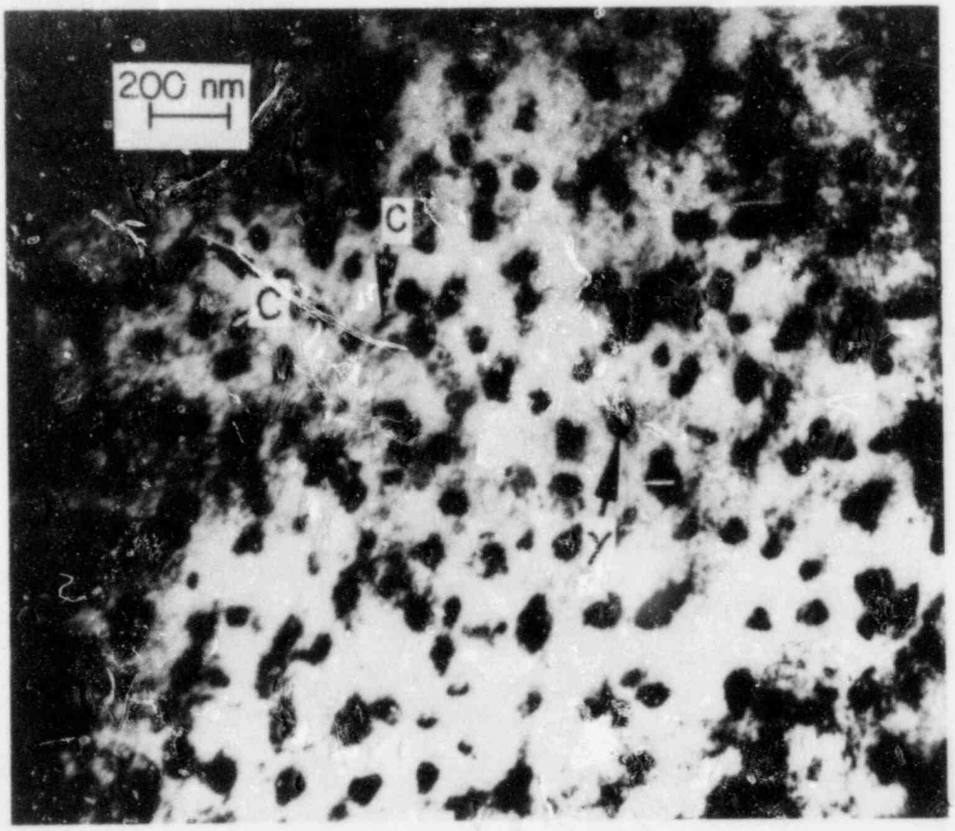

(A)

Fig. 2.1. TEM Micrographs Obtained from a Region Adjacent to the Brittle-Type Fracture Site of H. B. Robinson Cladding Tube 217A4G after Expanding-Mandrel Loading at 325°C. (A) Bright-field image showing precipitates; arrows denoted C and γ indicate cubic ZrO_2 and bulk hydride, respectively. (B) Indexed SAD pattern showing reflections of cubic ZrO_2, bulk hydride, artifact surface hydride, and α-Zr, each denoted by subscripts C, γ, χ, and α, respectively; (C, D, E) stereopairs of dark-field images produced from the reflections contained in aperture circles 3, 2, and 7, respectively, of (B). Stereopair (C) from circle 3 shows images from $(1\bar{1}3)$ reflections of the cubic ZrO_2, bulk hydride, and surface χ-hydride; stereopair (D) from circle 2 shows images from (002) reflections of the cubic ZrO_2, bulk hydride, and surface χ-hydride, as well as from the $(10\bar{1}1)$ reflection of α-Zr; stereopair (E) from circle 7 shows images from $(\bar{2}2\bar{2})$ reflections of the cubic ZrO_2, bulk hydride, and surface χ-hydride. Again, arrows C and γ indicate cubic ZrO_2 and bulk hydride, respectively; B and D in stereopair (C), for example, denote bulk and surface particles, respectively. The cubic ZrO_2 is generally spherical with a diameter of ~10 nm and occasionally forms aggregates resembling curved threads, as denoted by C arrows in (A), (C), (D), and (E).

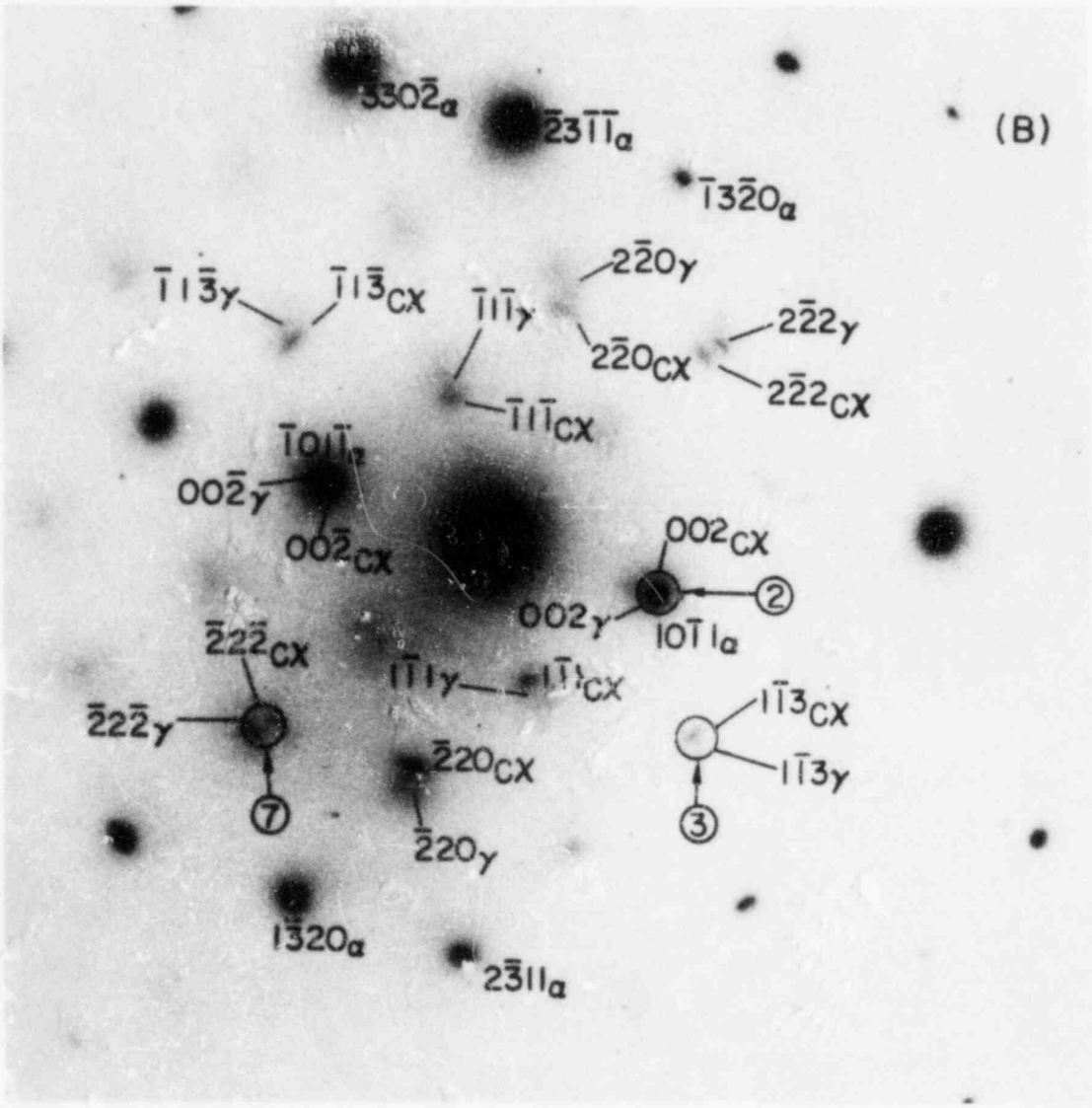
(B)
$33\bar{0}\bar{2}_\alpha$
$\bar{2}3\bar{1}\bar{1}_\alpha$
$\bar{1}3\bar{2}0_\alpha$
$\bar{1}1\bar{3}_\gamma$
$\bar{1}1\bar{3}_{CX}$
$\bar{1}11_\gamma$
$2\bar{2}0_\gamma$
$2\bar{2}0_{CX}$
$2\bar{2}2_\gamma$
$2\bar{2}2_{CX}$
$\bar{1}1\bar{1}_{CX}$
$\bar{1}01\bar{1}_\alpha$
$00\bar{2}_\gamma$
$00\bar{2}_{CX}$
002_{CX}
002_γ
$10\bar{1}1_\alpha$
②
$\bar{2}2\bar{2}_{CX}$
$\bar{2}2\bar{2}_\gamma$
⑦
$\bar{2}20_{CX}$
$\bar{2}20_\gamma$
$1\bar{3}20_\alpha$
$2\bar{3}11_\alpha$
$1\bar{1}3_{CX}$
$1\bar{1}3_\gamma$
③

Fig. 2.1. (Contd.)

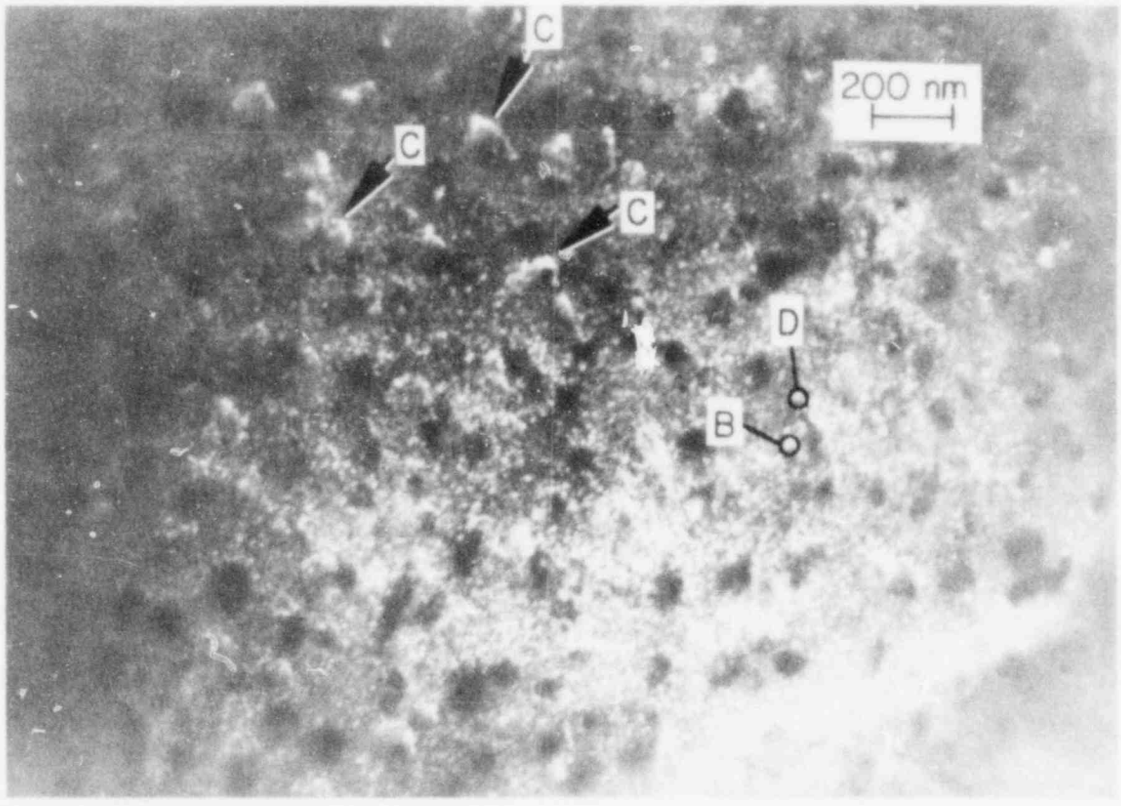

(C)

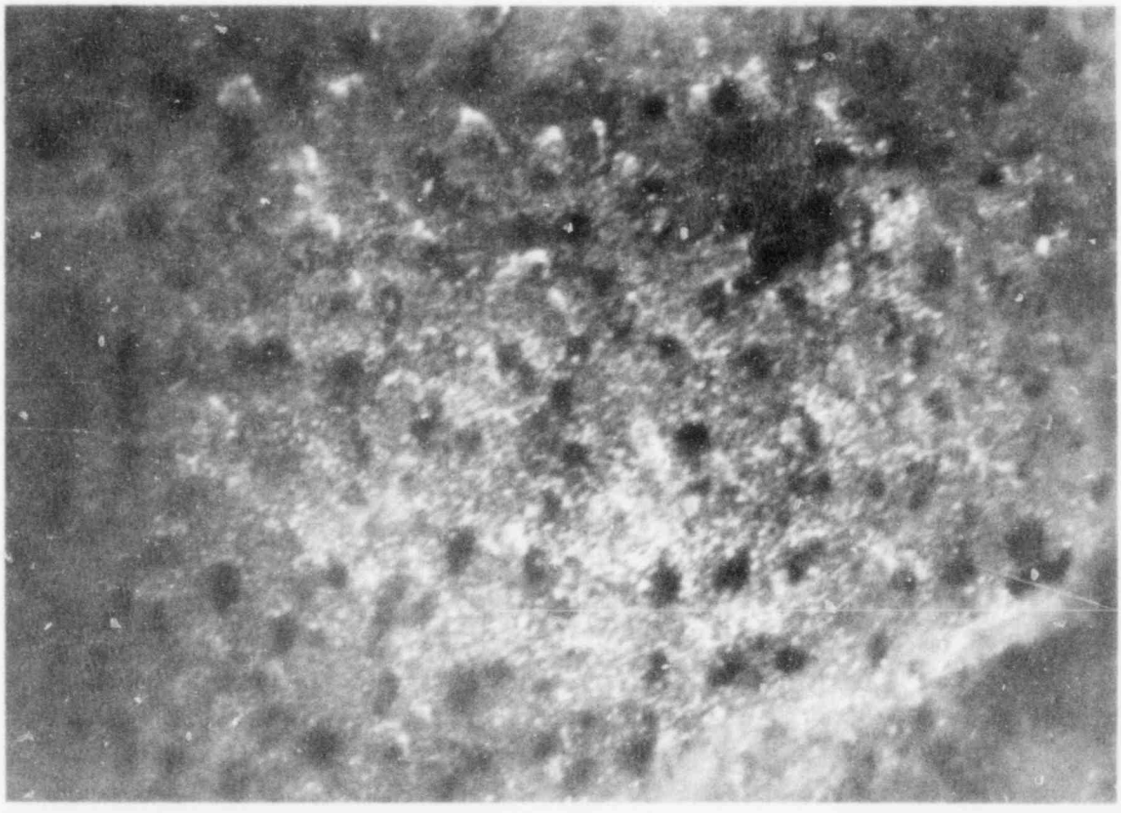

Fig. 2.1. (Contd.)

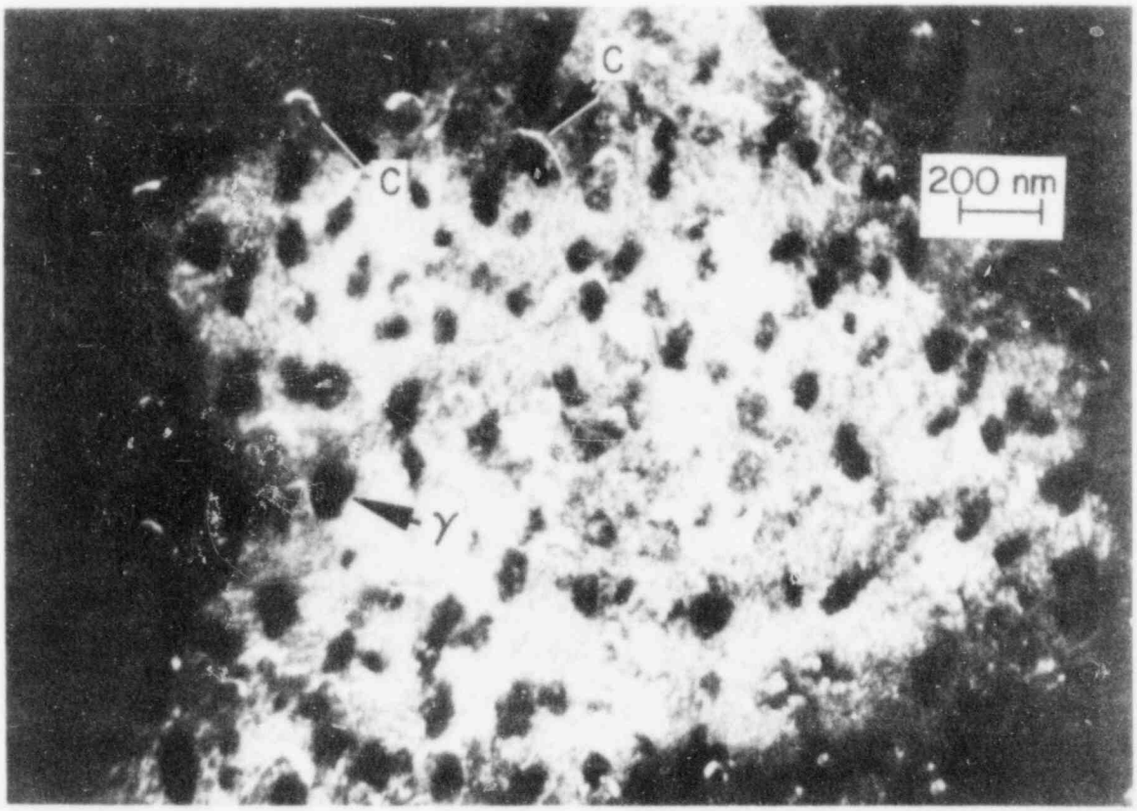

(D)

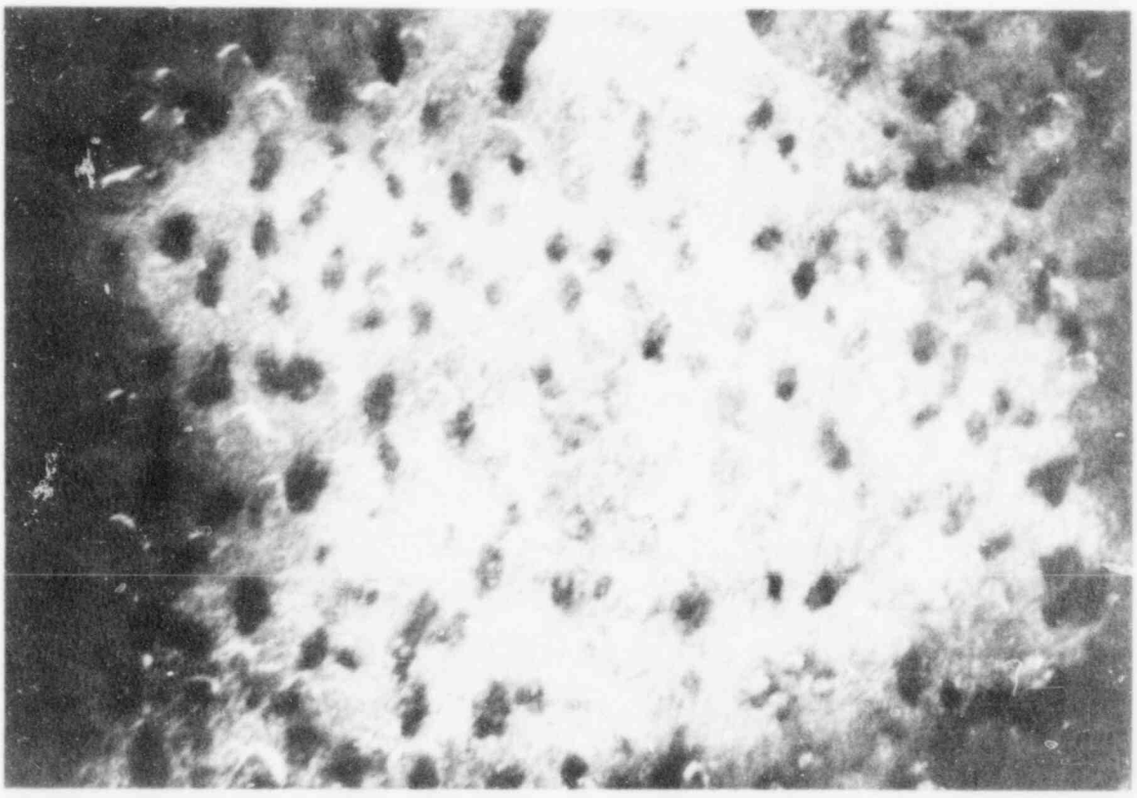

Fig. 2.1. (Contd.)

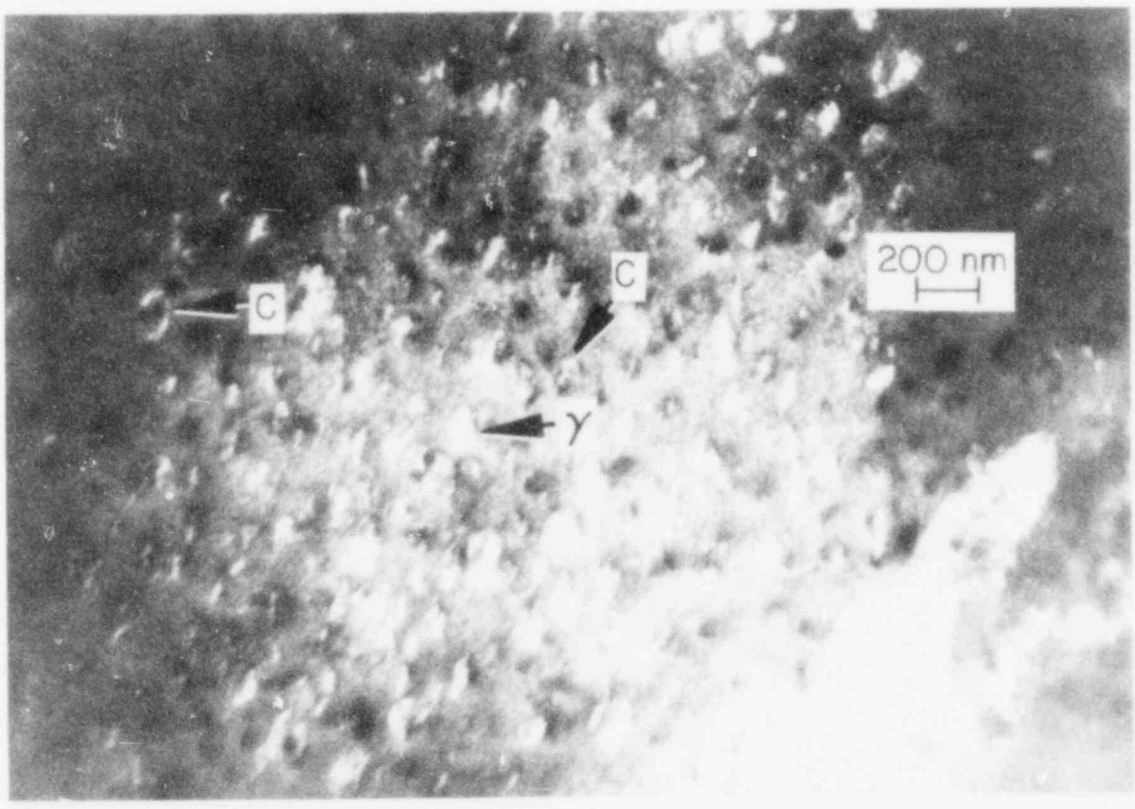

(E)

Fig. 2.1. (Contd.)

TABLE 2.1. Summary of Calculated Interplanar Spacings of Cubic-ZrO_2 Phase[a]

hkℓ	$h^2 + k^2 + \ell^2$	d (Å)
111	3	2.965
200	4	2.567
220	8	1.815
311	11	1.548
222	12	1.482
400	16	1.283
331	19	1.178
420	20	1.148
422	24	1.048
511, 333	27	0.988
440	32	0.907

[a]Space group Fm3m, fluorite structure with lattice parameter a_o = 0.5135 nm.

decreases and eventually vanishes.[4] This is similar to the behavior of superlattice reflections of the Zr_3O phase, which vanish with increased oxygen nonstoichiometry. For an approximate stoichiometry of ~$ZrH_{1.5}$, the fct γ-hydride transforms to fcc (a_o = 0.478 nm) δ-hydride. For a further excess of hydrogen atoms in the unit cell, ε-hydride, another fct phase with a c/a ratio smaller than unity, is observed at approximately the stoichiometry of ZrH_2. The sites occupied by the hydrogen atoms in the γ-, δ-, and ε-hydrides are limited to the tetrahedral interstices. However, some evidence has been reported which indicates hydrogen occupation of octahedral as well as the tetrahedral interstices for nonequilibrium hydrides.[5,6] The nonequilibrium artifact χ-hydride, which is produced during the jet-thinning of the thin-foil specimens, may well be associated with hydrogen occupation of the octahedral interstices.

The interplanar spacings of the γ- and δ-hydrides are summarized in Tables 2.3 and 2.4, respectively. Identification of the γ-hydride reflections is straightforward if the intensity of superlattice reflections is strong

TABLE 2.2. Summary of Calculated Interplanar Spacings of Surface χ-Hydride of Zirconium[a]

hkℓ	$h^2 + k^2$	ℓ^2	d (Å)
100	1	0	5.22
001	0	1	5.14
110	2	0	3.69
101	1	1	3.66
111	2	1	3.00
200	4	0	2.61
002	0	4	2.57
210	5	0	2.33
201	4	1	2.32
102	1	4	2.31
211	5	1	2.12
112	2	4	2.11
220	8	0	1.85
202	4	4	1.83
221	8	1	1.74
212	5	4	1.73
310	10	0	1.65
301	9	1	1.65
103	1	9	1.63
311	10	1	1.57
113	2	9	1.55
222	8	4	1.50
203	4	9	1.43
312	10	4	1.39
213	5	9	1.38
400	16	0	1.31
004	0	16	1.28
223	8	9	1.26
104	1	16	1.25
114	2	16	1.21
331	18	1	1.20
313	10	9	1.19
204	4	16	1.15
214	5	16	1.12

[a]Tetragonal with lattice parameters a_o = 0.522 nm and c_o = 0.514 nm.

TABLE 2.3. Summary of Calculated Interplanar Spacings of γ-Hydride of Zirconium[a]

hkℓ	$h^2 + k^2$	ℓ^2	d (Å)	Superlattice Reflection
110	2	0	3.242	x
111	2	1	2.722	
002	0	4	2.473	
200	4	0	2.292	
112	2	4	1.968	x
202	4	4	1.686	
220	8	0	1.624	
113	2	9	1.474	
310	10	0	1.452	x
311	10	1	1.389	
222	8	4	1.359	
312	10	4	1.252	x
004	0	16	1.241	
114	2	16	1.156	x
400	16	0	1.147	
313	10	9	1.093	
204	4	16	1.093	
331	18	1	1.057	
402	16	4	1.040	

[a]Space group $P4_2/n$, fct with a_o = 0.460 nm and c_o = 0.497 nm.

enough to be detectable. However, if the superlattice reflections are invisible, it is difficult to discern which hydride is present in the region that is being examined. This is because the differences between the interplanar spacings (see Tables 2.3 and 2.4) and angles are very small. The differences are difficult to detect from SAD patterns such as Fig. 2.1(B) since the hydride reflections are usually diffuse. Careful indexing of several different zones is required for a conclusive identification. For our present purpose, we will designate the phase simply as a bulk zirconium hydride, with the understanding that it is either γ- or δ-hydride.

A very useful technique for discernment of a bulk phase from a surface phase (such as the χ-hydride) is "$2\frac{1}{2}$D" microscopy.[7] When the dark-field image is slightly overfocused and underfocused in TEM, a slight

TABLE 2.4. Summary of Calculated Interplanar Spacings of δ-Hydride of Zirconium[a]

hkℓ	$h^2 + k^2 + \ell^2$	d (Å)
111	3	2.758
200	4	2.389
220	8	1.689
311	11	1.440
222	12	1.382
400	16	1.194
331	19	1.092
420	20	1.068
422	24	0.975
333	27	0.919
511	27	0.919
440	32	0.844
531	35	0.807

[a]fcc structure with lattice parameter a_o = 0.478 nm.

difference in the angles of the electron passage occurs. Therefore, the two images can be used effectively as stereopairs. By viewing the resulting micrographs with a stereoscope, a bulk and a surface phase can be readily discerned with this technique. Examples of dark-field stereopairs are shown in Figs. 2.1(C) and (D). The images of Fig. 2.1(C) were produced with $(1\bar{1}3)$ reflections of the cubic ZrO_2 as well as the χ-hydride. The two reflections are located at virtually identical spots. However, a stereoview of Fig. 2.1(C) clearly shows the bulk nature of the cubic-ZrO_2 precipitates and the surficial nature of the χ-hydride phase. The cubic-ZrO_2 particles shown in Fig. 2.1(C) have a diameter of ~10 nm and in many areas are aggregated in the form of curved threads as indicated by the arrows. In the case of Fig. 2.1(D), weak reflections from $(10\bar{1}1)_{\alpha\text{-Zr}}$ and (002) of the bulk hydride are superimposed on the (002) reflections of the cubic ZrO_2 and χ-hydride. Again, curved threads of cubic ZrO_2 are visible in Fig. 2.1(D).

The precipitates in dark contrast with a diameter of approximately 35-100 nm in Figs. 2.1(C) and (D) are the images of the bulk hydride that are produced as a result of leakage from the central beam. Because of the

leakage, they appear in the same contrast as in the bright-field image. The bulk-hydride morphology is visible more clearly in the bright-field image of Fig. 2.1(A). The nonsurficial nature of the hydride can be discerned from the stereopairs of Figs. 2.1(C) and (D). The dark-field stereopair of Fig. 2.1(E) shows dark-field images of $(\bar{2}2\bar{2})$ reflections of the cubic ZrO_2, bulk hydride, and surface χ-hydride. Again, visible in the figure are the leakage bright-field images of the cubic ZrO_2 and the bulk hydride.

Another example of stereopairs of dark-field images that reveal the nature and morphology of the cubic ZrO_2 and the bulk hydride is shown in Fig. 2.2. The thread-like morphology of cubic ZrO_2 is again visible in Fig. 2.2(C). In a similar stereopair of the dark-field images of Fig. 2.3(C), the χ-hydride reflections are absent. Instead, dark-field images of diffuse surface films, which are produced from the (111) reflection of monoclinic ZrO_2, are visible. Like the χ-hydride, the monoclinic-ZrO_2 phase is a surface artifact, and, consequently, is not associated with the fracture behavior of the specimen.

The bulk hydride shown in Figs. 2.1-2.3 is not the same as the δ-hydride metallographically observed in most of the spent-fuel cladding materials. As shown in Fig. 48 of Ref. 8, the δ-hydride is bar-like in shape, with a length of the order of ~1000 nm. As a result, it is readily observed in optical micrographs. In contrast, the bulk hydrides shown in Figs. 2.1-2.3 are too small to be observable in either optical or SEM micrographs. However, the role of the smaller hydrides in the deformation and fracture of the specimen at 325°C is not entirely clear, since at that temperature the hydride itself may be ductile. Nevertheless, the bulk cubic-ZrO_2 precipitates will profoundly limit the plastic deformation of the material at the same temperature.

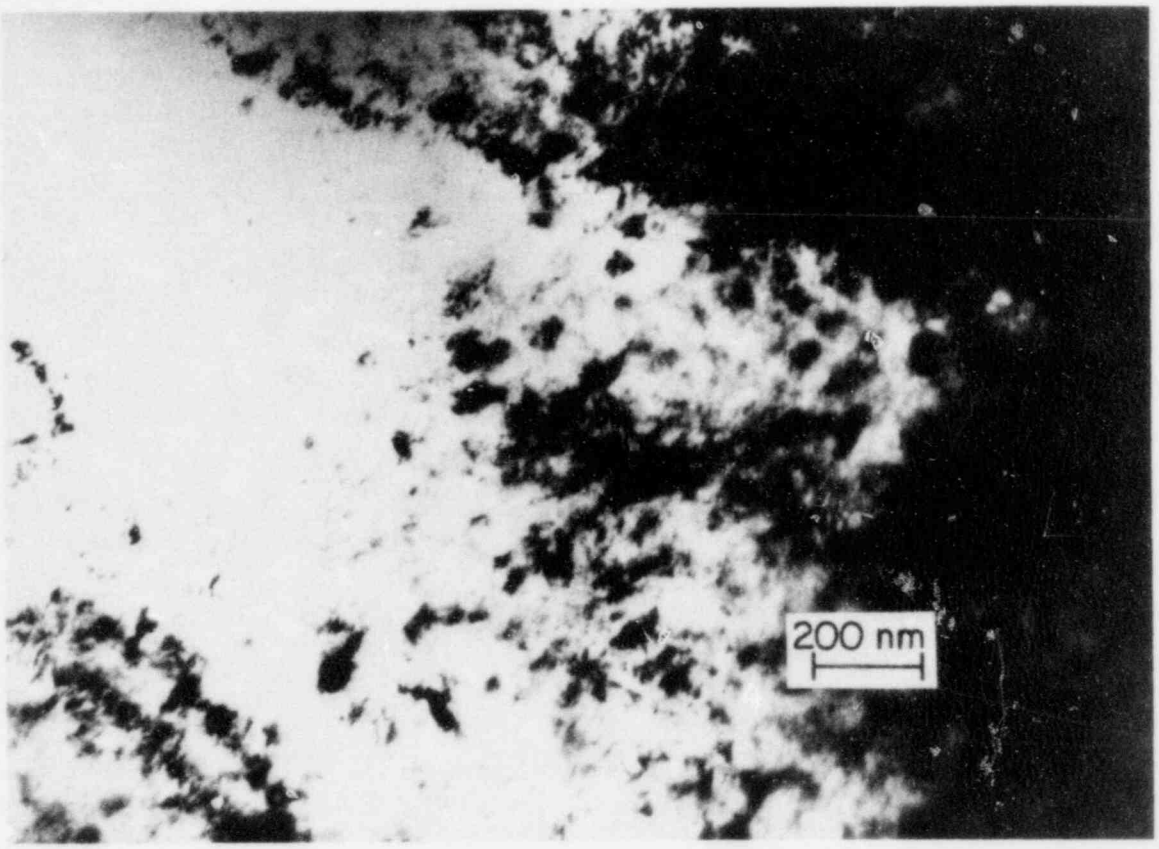

(A)

Fig. 2.2. TEM Micrographs Similar to Fig. 2.1. (A) Bright-field image; (B) indexed SAD pattern; (C, D) stereopairs of dark-field images. Stereopair (C) shows images from $(2\bar{2}0)$ reflections of cubic ZrO_2 and χ-hydride, and $(\bar{1}\bar{1}20)$ reflection of α-Zr; stereopair (D) shows images from $(1\bar{1}\bar{1})$ reflections of cubic ZrO_2, bulk hydrides, and surface χ-hydrides.

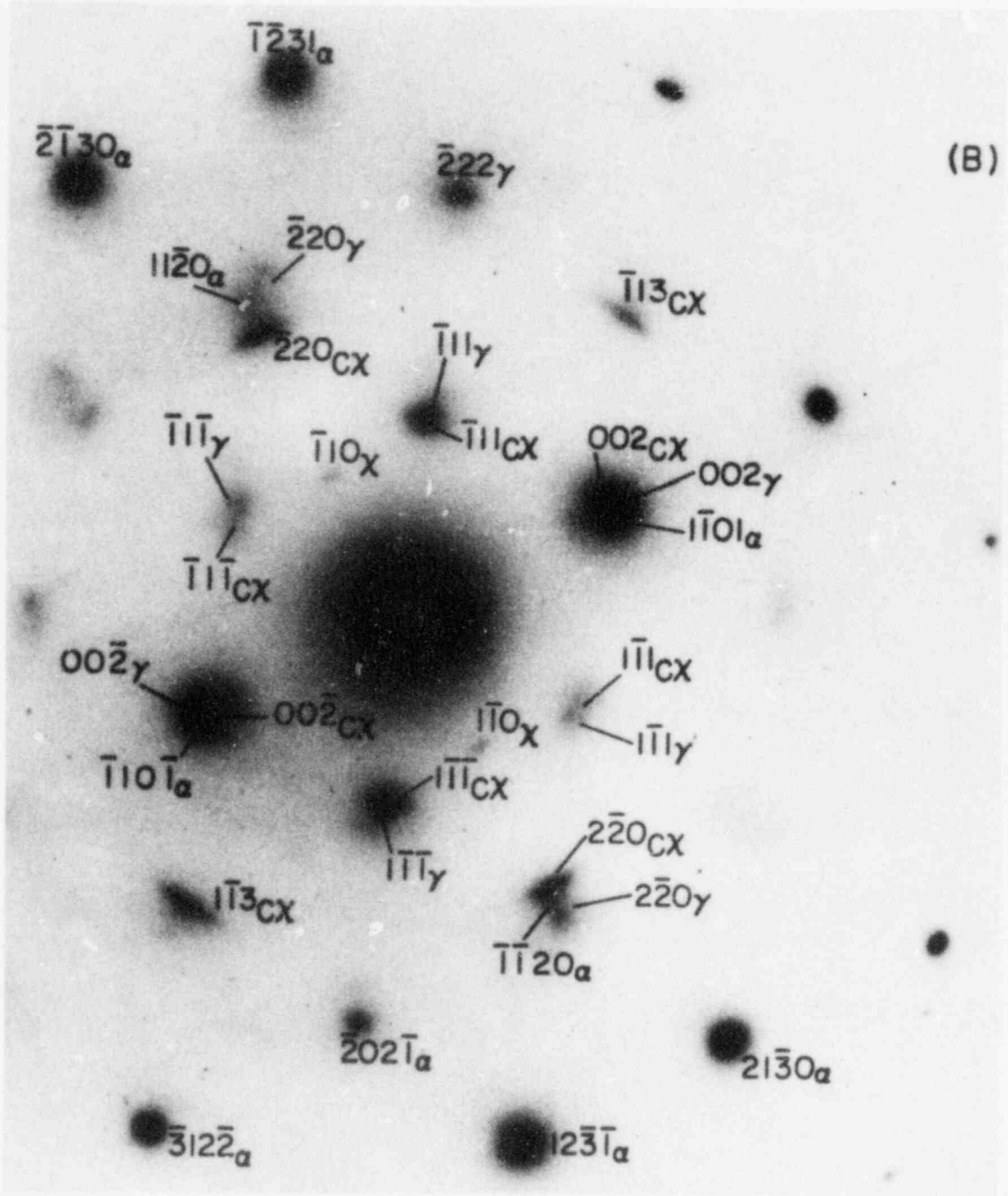
$\bar{1}\bar{2}3\bar{1}_\alpha$
$\bar{2}\bar{1}3\bar{0}_\alpha$
$\bar{2}22_\gamma$
(B)
$\bar{2}20_\gamma$
$11\bar{2}0_\alpha$
$\bar{1}13_{CX}$
220_{CX}
$\bar{1}11_\gamma$
$\bar{1}\bar{1}\bar{1}_\gamma$
$\bar{1}10_X$
$\bar{1}11_{CX}$
002_{CX}
002_γ
$1\bar{1}01_\alpha$
$\bar{1}\bar{1}\bar{1}_{CX}$
$00\bar{2}_\gamma$
$1\bar{1}1_{CX}$
$00\bar{2}_{CX}$
$1\bar{1}0_X$
$1\bar{1}\bar{1}_\gamma$
$\bar{1}10\bar{1}_\alpha$
$1\bar{1}\bar{1}_{CX}$
$2\bar{2}0_{CX}$
$1\bar{1}\bar{1}_\gamma$
$2\bar{2}0_\gamma$
$1\bar{1}3_{CX}$
$\bar{1}\bar{1}20_\alpha$
$\bar{2}02\bar{1}_\alpha$
$21\bar{3}0_\alpha$
$\bar{3}122_\alpha$
$123\bar{1}_\alpha$

Fig. 2.2. (Contd.)

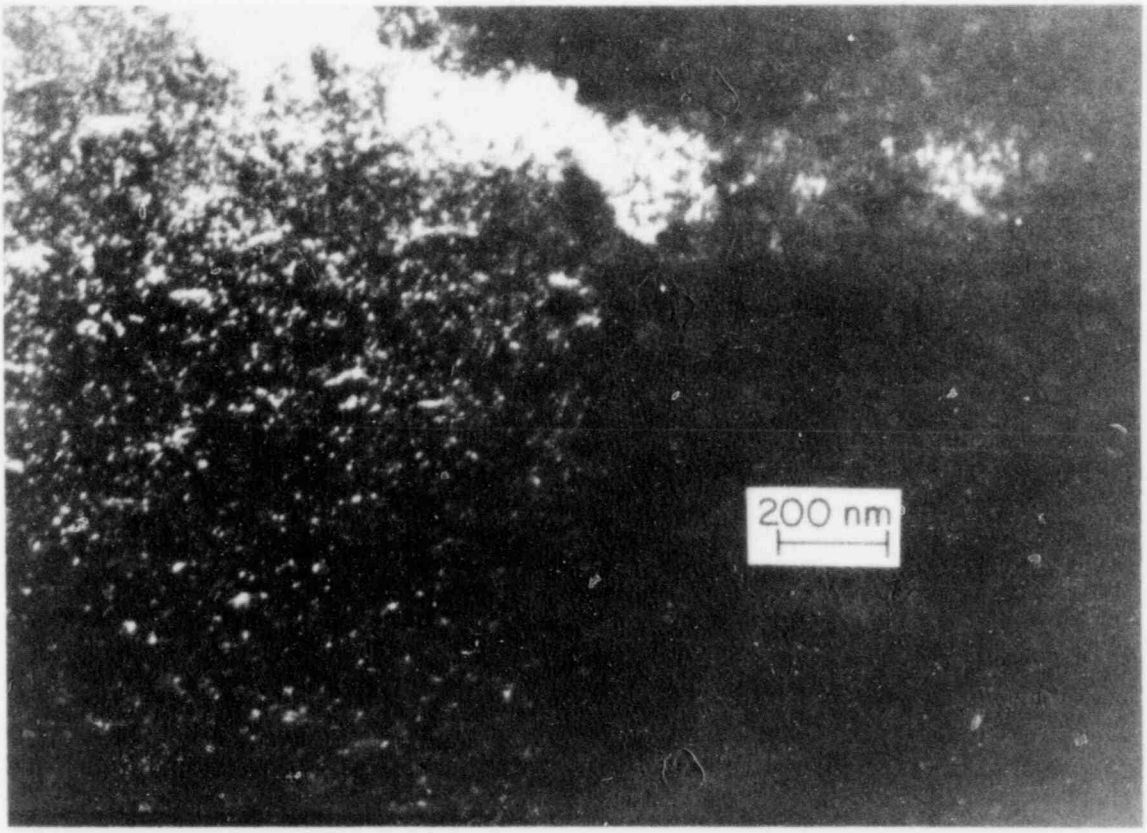

(C)

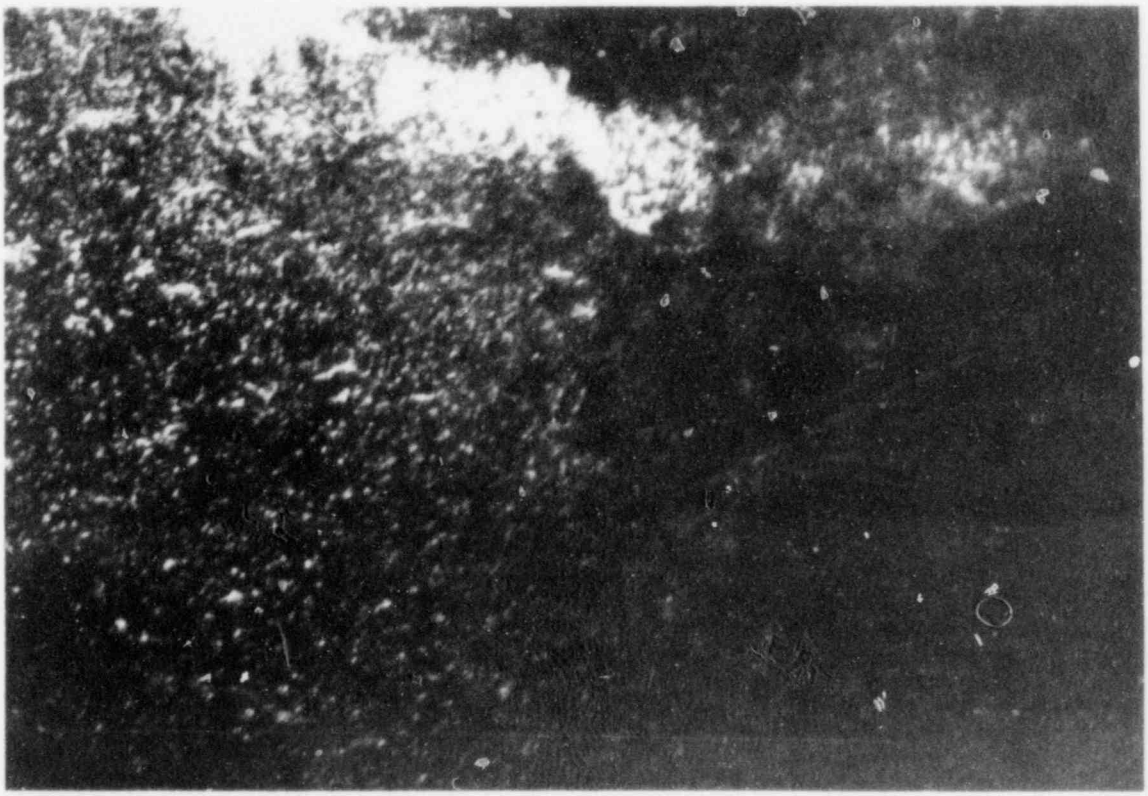

Fig. 2.2. (Contd.)

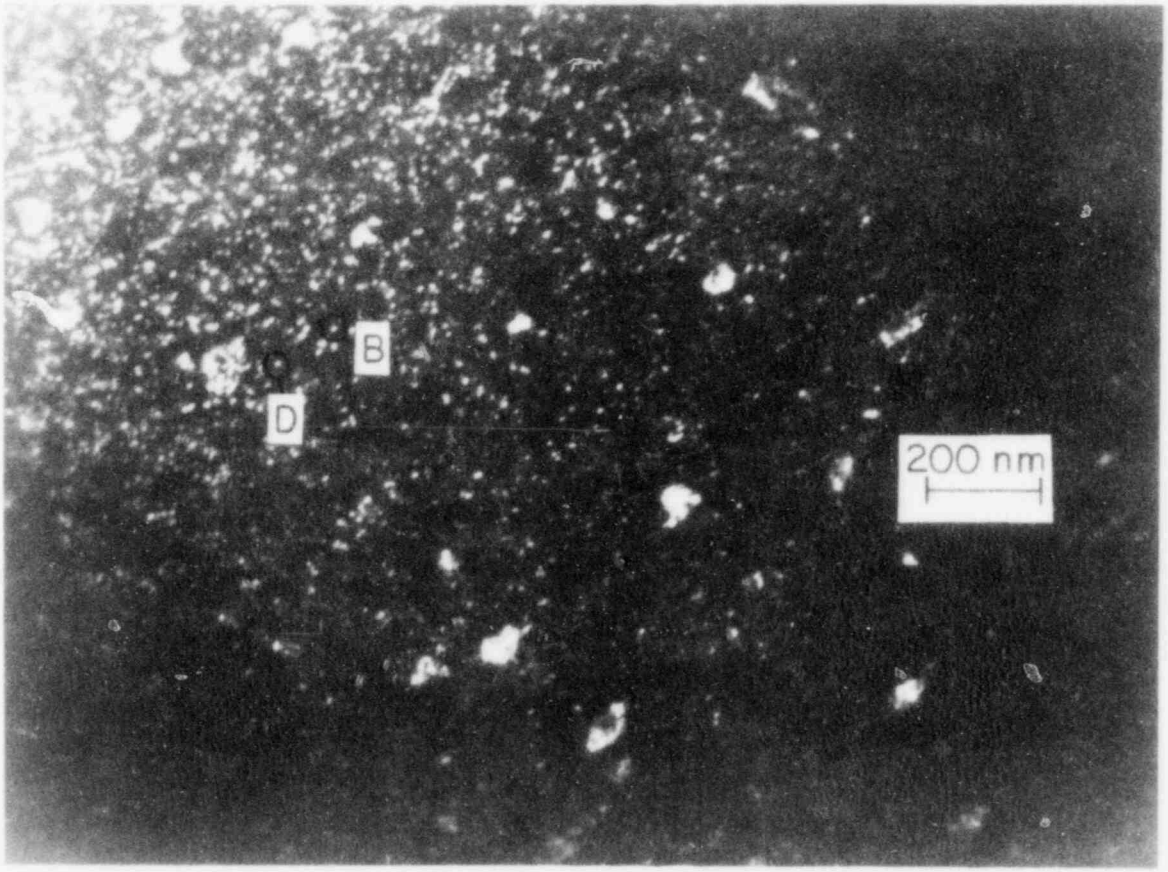

(D)

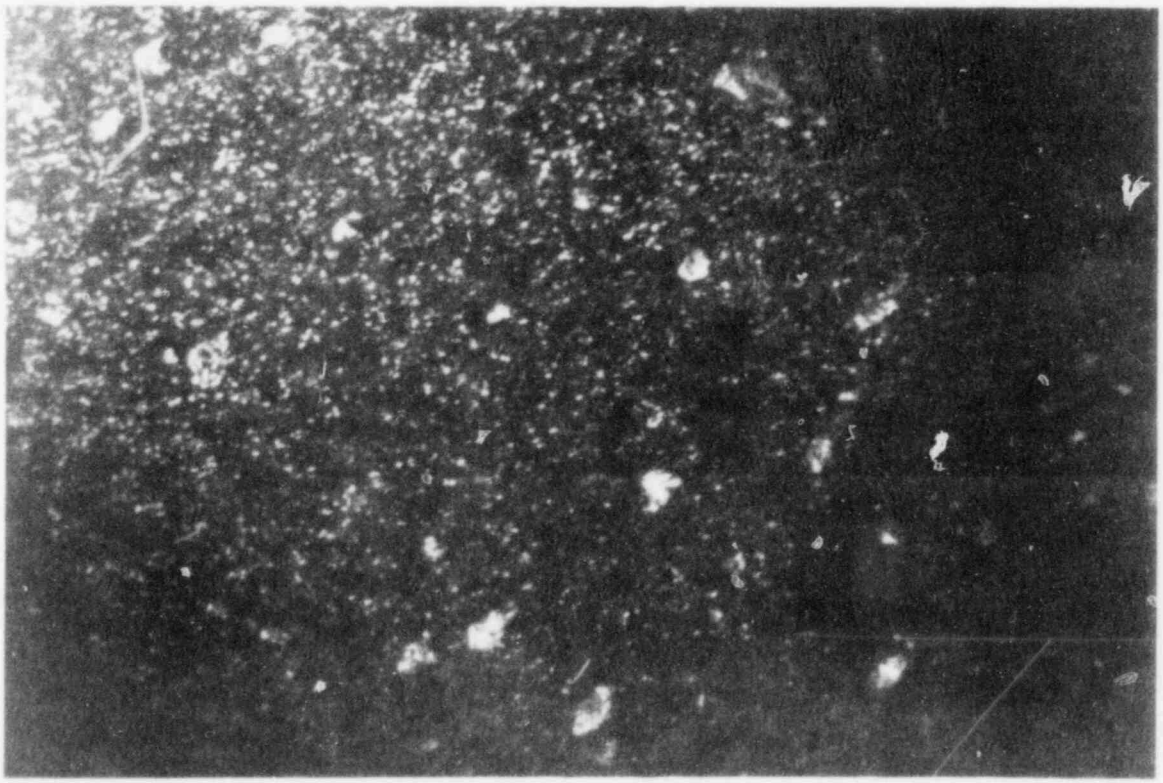

Fig. 2.2. (Contd.)

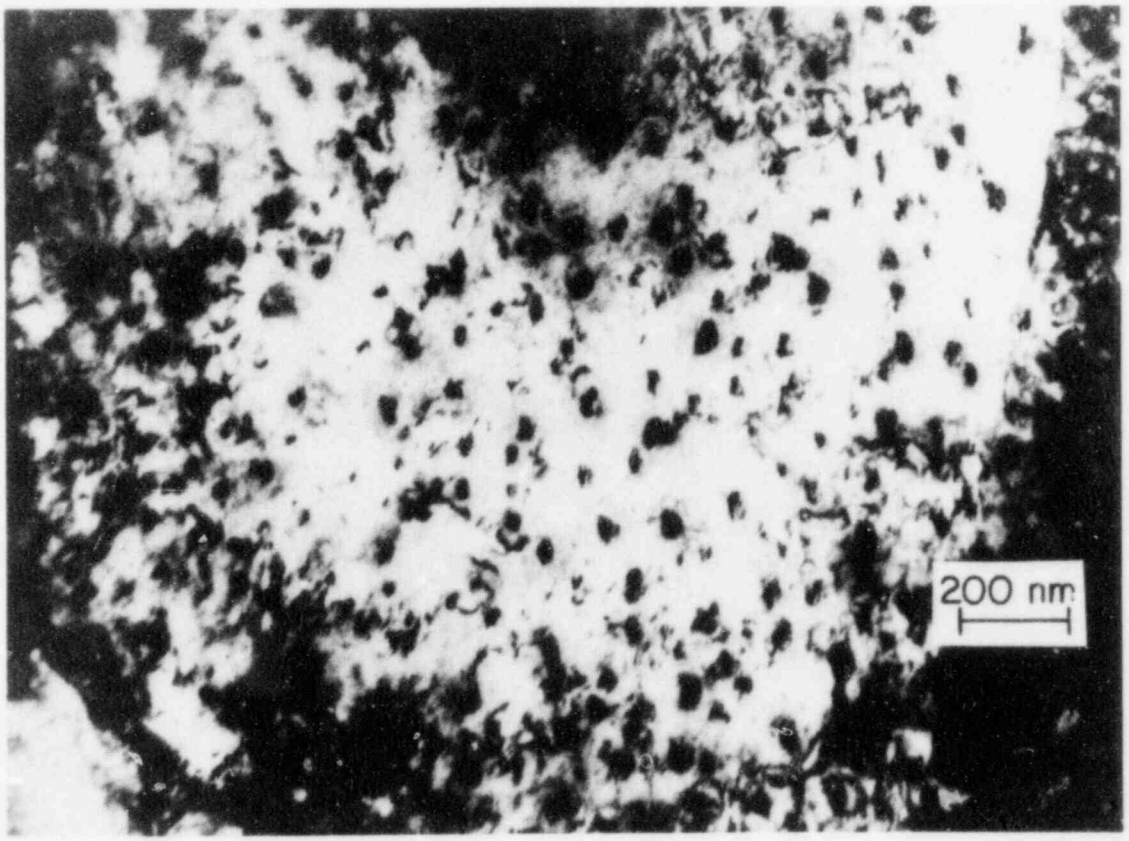

(A)

Fig. 2.3. TEM Micrographs Similar to Fig. 2.1. (A) Bright-field image; (B) indexed SAD pattern; and (C) stereopair of dark-field images produced from ($\bar{1}11$) reflections of the cubic ZrO_2 (small particles ~10 nm in size), bulk hydride (large precipitates ~30 nm in size), and (111) reflection of the surface monoclinic ZrO_2 (diffuse film).

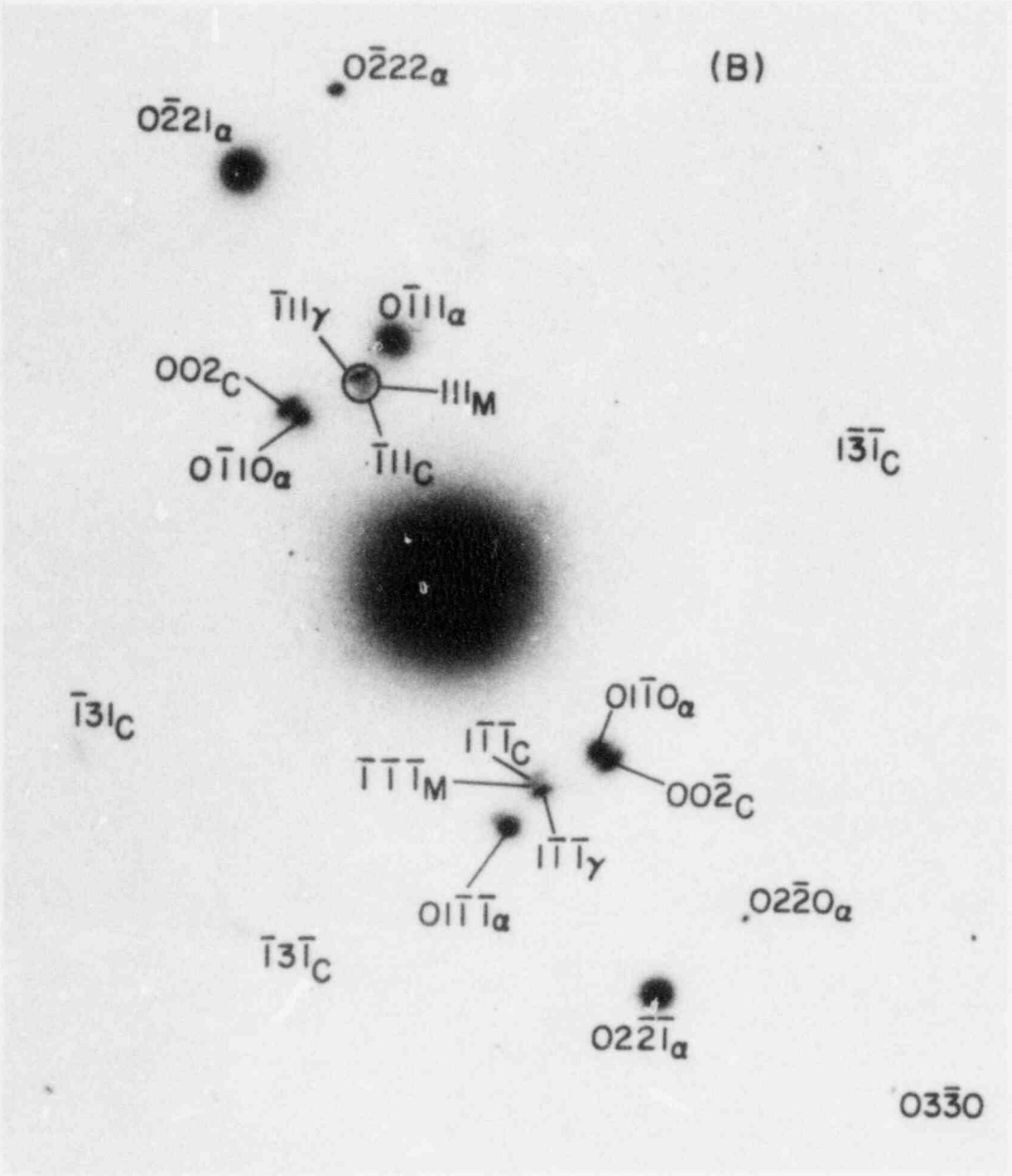
(B)
$0\bar{2}22_\alpha$
$0\bar{2}21_\alpha$
$\bar{1}11_\gamma$
$0\bar{1}11_\alpha$
002_C
111_M
$0\bar{1}10_\alpha$
$\bar{1}11_C$
$1\bar{3}\bar{1}_C$
$\bar{1}31_C$
$01\bar{1}0_\alpha$
$1\bar{1}\bar{1}_C$
$\bar{1}\bar{1}\bar{1}_M$
$00\bar{2}_C$
$1\bar{1}\bar{1}_\gamma$
$011\bar{1}_\alpha$
$02\bar{2}0_\alpha$
$\bar{1}3\bar{1}_C$
$02\bar{2}\bar{1}_\alpha$
$03\bar{3}0$

Fig. 2.3. (Contd.)

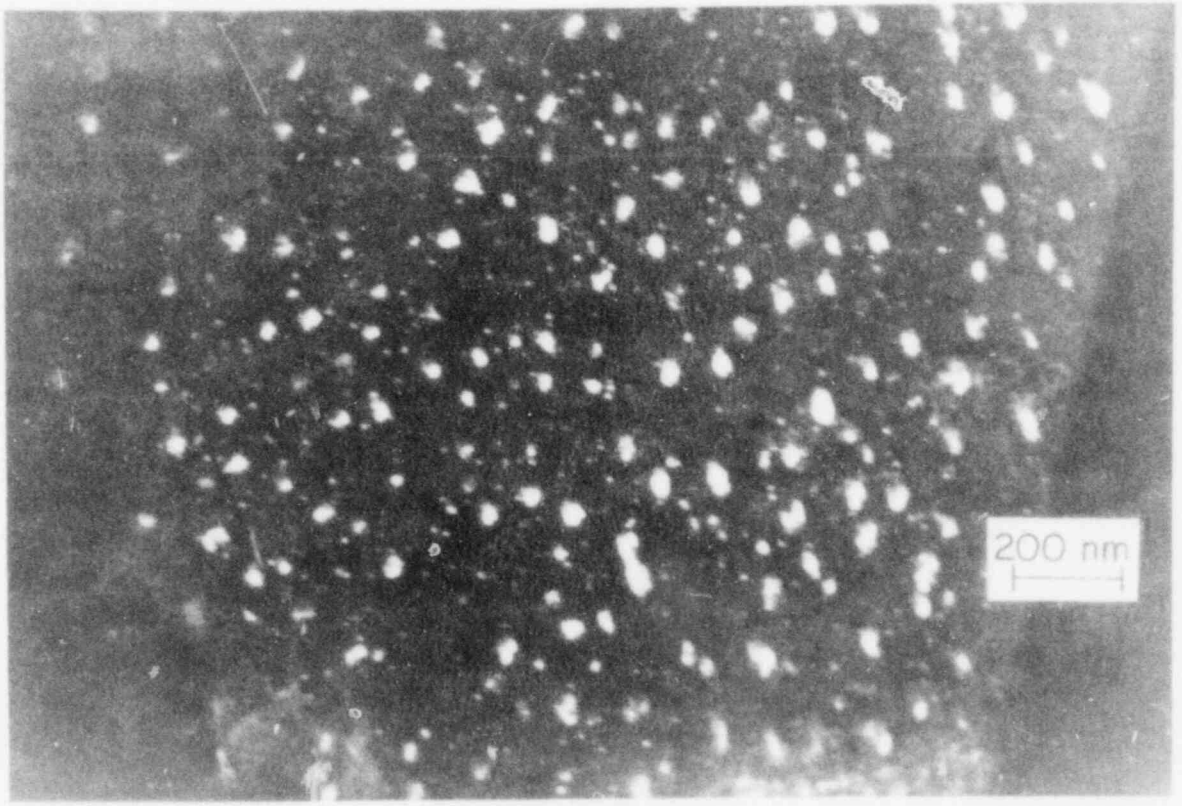

(C)

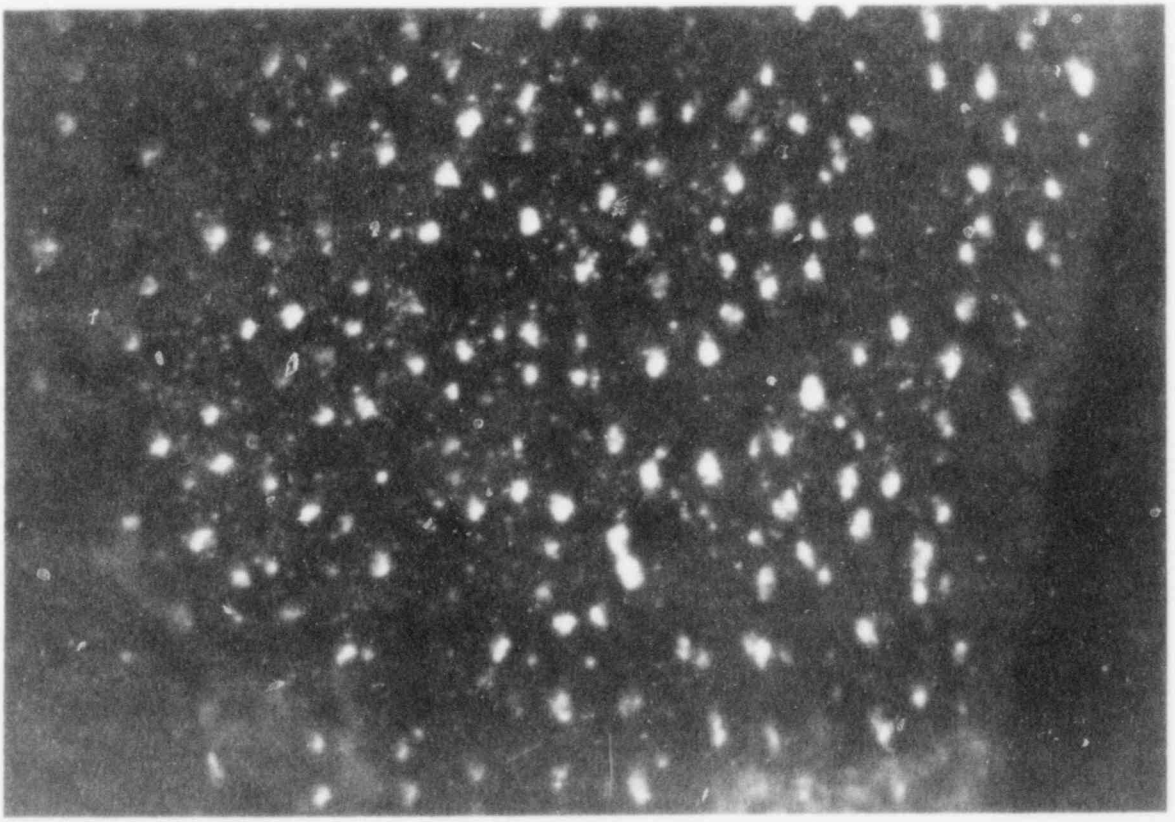

Fig. 2.3. (Contd.)

B. References for Chapter II

1. H. M. Chung, in Light-Water-Reactor Safety Fuel Systems Research Programs: Quarterly Progress Report, April-June 1984, NUREG/CR-3980 Vol. II, ANL-84-61 Vol. II (February 1985), pp. 12-24.
2. R. W. G. Wyckoff, in Crystal Structures, 2nd Ed., Vol. 1, Interscience Publishers, 1963, pp. 239-246.
3. H. M. Chung, "TEM-HVEM Observation of Ordered Zirconium-Oxygen Phase in Zircaloy Spent-Fuel Cladding," in Proc. Intl. Symp. on Environmental Degradation of Materials in Nuclear Power Systems - Water Reactors, Myrtle Beach, SC, August 22-24, 1983, pp. 297-333.
4. S. S. Sidhu, L. R. Heaton, F. P. Campos, and D. D. Zauberis, Adv. Chem. Series 39, 87 (1963).
5. E. F. Khodosov, Fiz. Met. Metalloved. 29, 415 (1970).
6. V. F. Petrunin, S. K. Dolukhanyan, M. G. Zemlyanov, S. V. Marchenko, and P. P. Parshin, Positions of Hydrogen Atoms in Zirconium Hydride, Sov. Phys. Solid State 23, 1126 (1981).
7. W. L. Bell, $2\frac{1}{2}$D Electron Microscopy: Through-Focus Dark-Field Image Shifts, J. Appl. Phys. 47, 1676 (1976).
8. H. M. Chung, in Materials Science Division Light-Water-Reactor Safety Research Program: Quarterly Progress Report, January-March 1982, NUREG/CR-2970 Vol. I, ANL-82-41 Vol. I (October 1982), pp. 80-97.

Distribution for NUREG/CR-3980 Vol. III (ANL-84-61 Vol. III)

Internal:

R. Avery
O. K. Chopra
H. M. Chung
L. W. Deitrich
C. E. Dickerman
G. R. Fenske
F. Y. Fradin
B. R. T. Frost
E. E. Gruber
G. L. Hofman
M. Ishii
W. D. Jackson
C. E. Johnson
T. F. Kassner (10)
K. L. Kliewer
J. M. Kramer
D. S. Kupperman
D. J. Lam
Y. Y. Liu
P. A. Lottes
P. S. Maiya
K. Natesan
L. A. Neimark
F. A. Nichols
P. R. Okamoto
R. G. Palm
J. Y. Park
R. B. Poeppel
L. E. Rehn
J. Rest (10)
W. E. Ruther
R. A. Scharping
W. J. Shack (3)
E. M. Stefanski (2)
R. V. Strain
C. E. Till
H. C. Tsai
R. A. Valentin
A. Villalobos
R. W. Weeks
H. Wiedersich
F. L. Yaggee
ANL Patent Dept.
ANL Contract File
ANL Libraries (3)
TIS Files (6)

External:

NRC, for distribution per R3 (275)
DOE-TIC (2)
Manager, Chicago Operations Office, DOE
R. Tom, DOE-CH
Materials Science and Technology Division Review Committee:
C. B. Alcock, U. Toronto
A. Arrott, Simon Fraser U.
R. C. Dynes, Bell Labs., Murray Hill
A. G. Evans, U. California, Berkeley
H. K. Forsen, Bechtel National, Inc., San Francisco
E. Kay, IBM San Jose Research Lab.
M. B. Maple, U. California, San Diego
P. G. Shewmon, Ohio State U.
J. K. Tien, Columbia U.
J. W. Wilkins, Cornell U.
R. B. Adamson, General Electric Co., Vallecitos Nuclear Center, P. O. Box 460, Pleasanton, Calif. 94566
P. L. Andresen, General Electric Corporate Research and Development, Schenectady, N. Y. 12301
G. A. Arlotto, Office of Nuclear Regulatory Research, USNRC, Washington
D. Atteridge, Battelle Pacific Northwest Lab., P. O. Box 999, Richland, Wash. 99352
D. L. Burman, Westinghouse PWR Systems Div., P. O. Box 355, Pittsburgh, Pa. 15230
L. K. Chan, Office of Nuclear Regulatory Research, USNRC, Washington
B. Cox, Chalk River Nuclear Labs., AECL, Chalk River, Ont., K0J 1J0, Canada
R. B. Foulds, Office of Nuclear Reactor Regulation, USNRC, Washington
S. M. Gehl, Electric Power Research Inst., P. O. Box 10412, Palo Alto, Calif. 94304
J. H. Gittus, Springfields Nuclear Power Development Labs., U. K. Atomic Energy Authority, Springfields, Salwick, Preston, PR4 ORR, England
R. R. Hobbins, EG&G/INEL, 1520 Sawtelle Dr., Idaho Falls, Idaho 83401
W. V. Johnston, Office of Nuclear Reactor Regulation, USNRC, Washington

R. L. Jones, Electric Power Research Inst., P. O. Box 10412, Palo Alto, Calif. 94304
K. R. Jordan, Nuclear Fuel Div., Monroeville Nuclear Center, Westinghouse Electric Corp., Monroeville, Pa. 15146
C. N. Kelber, Office of Nuclear Regulatory Research, USNRC, Washington
E. Kohn, Atomic Energy of Canada Ltd., Sheridan Park Research Community, Mississauga, Ont., Canada L5K 1B2
P. M. Lang, Office of Converter Reactor Deployment, USDOE, Washington, D. C. 20545
D. D. Lanning, Battelle Pacific Northwest Lab., P. O. Box 999, Richland, Wash. 99352
R. A. Lorenz, Oak Ridge National Lab., P. O. Box X, Oak Ridge, Tenn. 37830
P. MacDonald, EG&G/INEL, 1520 Sawtelle Dr., Idaho Falls, Idaho 83401
G. P. Marino, Office of Nuclear Regulatory Research, USNRC, Washington
S. McDonald, Westinghouse Electric Corp., R&D Center, Beulah Rd., Pittsburgh, Pa. 15235
K. R. Merckx, Exxon Nuclear, Inc., 2955 George Washington Way, Richland, Wash. 99352
A. C. Millunzi, Office of Nuclear Energy, USDOE, Washington, D. C. 20545
D. R. O'Boyle, Commonwealth Edison Co., P. O. Box 767, Chicago, Ill. 60690
R. N. Oehlberg, Electric Power Research Inst., P. O. Box 10412, Palo Alto, Calif. 94304
M. F. Osborne, Oak Ridge National Lab., P. O. Box X, Oak Ridge, Tenn. 37830
D. E. Owen, EG&G Idaho, P. O. Box 88, Middletown, Pa. 17057
T. P. Papazoglou, Lynchburg Research Center, Babcock & Wilcox Co., P. O. Box 1260, Lynchburg, Va. 24505
J. T. A. Roberts, Electric Power Research Inst., P. O. Box 10412, Palo Alto, Calif. 94304
H. H. Scott, Office of Nuclear Regulatory Research, USNRC, Washington
R. D. Silver, Office of Nuclear Reactor Regulation, USNRC, Washington
P. Smerd, Combustion Engineering, Inc., P. O. Box 500, Windsor, Conn. 06095
A. A. Solomon, School of Nuclear Engineering, Purdue U., West Lafayette, Ind. 47907
R. Van Houten, Office of Nuclear Regulatory Research, USNRC, Washington

NRC FORM 335 (2 84) NRCM 1102, 3201, 3202

U.S. NUCLEAR REGULATORY COMMISSION

BIBLIOGRAPHIC DATA SHEET

SEE INSTRUCTIONS ON THE REVERSE

1 REPORT NUMBER (Assigned by TIDC add Vol. No., if any)

NUREG/CR-3980 Vol. III
ANL-84-61 Vol. III

2 TITLE AND SUBTITLE

Light-Water-Reactor Safety Fuel Systems Research Programs: Quarterly Progress Report, July-September 1984

3 LEAVE BLANK

4 DATE REPORT COMPLETED

MONTH	YEAR
April	1985

5 AUTHOR(S)

J. Rest et al.

6 DATE REPORT ISSUED

MONTH	YEAR
April	1985

7 PERFORMING ORGANIZATION NAME AND MAILING ADDRESS (Include Zip Code)

Argonne National Laboratory
9700 South Cass Avenue
Argonne, Illinois 60439

8 PROJECT/TASK/WORK UNIT NUMBER

9 FIN OR GRANT NUMBER

A2016, A2017

10 SPONSORING ORGANIZATION NAME AND MAILING ADDRESS (Include Zip Code)

Division of Accident Evaluation
Office of Nuclear Regulatory Research
U. S. Nuclear Regulatory Commission
Washington, D. C. 20555

11a TYPE OF REPORT

Technical

b PERIOD COVERED (Inclusive dates)

July-September 1984

12 SUPPLEMENTARY

13 ABSTRACT (200 words or less)

This progress report summarizes the Argonne National Laboratory work performed during July, August, and September 1984 on water reactor safety problems related to fuel and fuel cladding materials. The research and development areas covered are Transient Fuel Response and Fission Product Release and Clad Properties for Code Verification.

14 DOCUMENT ANALYSIS - a KEYWORDS/DESCRIPTORS

fission product modeling
fission product release
irradiated Zircaloy cladding
mandrel loading tests
Zircaloy fracture
Zr_3O precipitation

b IDENTIFIERS/OPEN ENDED TERMS

15 AVAILABILITY STATEMENT

Unlimited

16 SECURITY CLASSIFICATION

(This page) Unclassified

(This report) Unclassified

17 NUMBER OF PAGES

50

18 PRICE